The intermediate step in fractionation trends of mildly alkaline volcanic suites: An experimental insight from the Pavin trachyandesite (Massif Central, France)

Morgane Rondet, Caroline Martel, Jean-Louis Bourdier

The intermediate step in fractionation trends of mildly alkaline volcanic suites: an experimental insight from the Pavin trachyandesite (Massif Central, France)

Morgane RONDET, Caroline MARTEL, Jean-Louis BOURDIER

Institut des Sciences de la Terre d'Orléans (ISTO), Université d'Orléans-CNRS-BRGM, Orléans, France

Abstract

We examined magma storage conditions and eruptive dynamics for the trachyandesite (~58 wt% SiO_2, 9-10 wt% alkalis) of the Pavin monogenetic volcano, a maar-like explosive crater belonging to a small group of youngest volcanoes in the Massif Central. By confronting the natural samples to experimental products, we constrained pre-eruptive conditions around 950-975 °C, 150-200 MPa (~5.5-7.0 km in depth), NNO+1.5, and 4.5-5.5 wt% melt H_2O. There is petrological evidence of magma crystallization in the conduit up to shallow levels (~50 MPa; 2 km deep) before fragmentation into pumice clasts in the last km of ascent. The experiments highlight the role of biotite and crystallization pressure in defining separate compositional trends of residual liquids, i.e. alkaline (trachytes) versus sub-alkaline (dacite-rhyolite).

Keywords: trachyandesite; Pavin; experimental petrology; differentiation.

1. Introduction

The Tertiary to Quaternary volcanic province of the Massif Central (France) is part of an intraplate alkaline volcanism, the Cenozoic European Volcanic Province (CEVP) that spreads from Spain to Poland and is spatially associated with a large-scale rift system surrounding the Alps orogen. Rifting and volcanism globally formed due to local extension and mantle upwelling in response to the Alpine orogeny (Lustrino and Wilson, 2007, and references therein). In the Massif Central, discrete volcanic fields are recognized based on spatiotemporal criteria, ranging in age mostly from the Middle Miocene to the Holocene. Most of those fields are uniquely basaltic, while some erupted magmas of intermediate compositions, i.e. trachyandesites *s.l.* and/or phonolites, along with subordinate volumes of trachytes (Velay,

Cantal, Chaîne des Puys) and even rhyolites (Monts Dore) (e.g. Brousse, 1961; Downes, 1987). Comparable alkaline suites with differentiated terms have been documented in other segments of the CEVP, notably the Upper Rhine Valley (e.g. Schreiber et al., 1999; Wörner et al., 1983), and the Bohemian Massif (Ulrych et al., 1999; Ackerman et al., 2015). The differentiated terms of the CEVP suites have been largely interpreted as resulting from polybaric differentiation of variously silica under-saturated primary mafic magmas by assimilation-fractional crystallization (AFC) processes ending in the upper crust. Such a case has been made for the Massif Central magmatic suites: Cantal (Downes, 1984 ; Wilson et al., 1995), Monts Dore (Briot et al., 1991), and Velay and Chaîne des Puys (Villemant, 1979 ; Maury et al., 1980 ; Villemant et al., 1981). Crystal fractionation trends in those suites have been defined mainly from the mineral assemblages of the various terms of the suites, and on mass-balance calculations using major and trace elements. However, constraints by phase- equilibrium experiments on the storage conditions and fractionation paths of such mildly alkaline, intermediate and silicic magmas remain currently scarce. A previous experimental study (Martel et al., 2013) investigated the storage conditions of trachytic magmas from the youngest volcanic field in the Massif Central, i.e. the partly Holocene Chaîne des Puys. In the present paper, we go back to an intermediate step in the differentiation trend by examining phase-equilibrium conditions for a representative trachyandesite (~58 wt% SiO_2) taken from the neighbouring Holocene Pavin volcano. Pavin is a maar-like explosive crater belonging to a small group of youngest volcanoes in the Massif Central, i.e. slightly younger than the Chaîne des Puys volcanoes, and located only about 40 km South of them in a similar tectonic setting. The aim of this study is (1) to constrain the storage conditions of the Pavin trachyandesite, erupted from a likely small-volume reservoir ; (2) to investigate the conditions that can generate trachytic liquids (such as those of the Chaîne des Puys) from a trachyandesitic parent by crystal fractionation.

2. Geological setting and sampling

The Pavin volcano is a roughly circular explosive crater 900-1000 m in diameter, filled by a crater lake about 750 m in diameter and 92 m maximum depth. The crater rim crosscuts lava flows from an adjacent scoria cone, the Montchal volcano. Four kilometers South, stands another morphologically well-preserved scoria cone, the Montcineyre volcano. At least one neighbouring maar, Estivadoux, is demonstrated by typical phreatomagmatic basaltic deposits

exposed in its surroundings, though it is currently buried by Montchal scoria flows and proximal Pavin deposits. Therefore, Pavin belongs to a small group of at least four recent monogenetic volcanoes (the Pavin group herein; Fig. 1), whose tephrostratigraphical and field relationships unambiguously define the relative eruption chronology as Montcineyre- Estivadoux-Montchal-Pavin, from the oldest to the youngest (Bourdier, 1980). The lack of paleosoil and the erosive contact between tephra layers from those volcanoes strongly suggest eruption within a short period of time. The most recent radiometric assessment gives an age of 4720 ±170 B.C. (current age of 6730 ±170) for the Pavin eruption, and a time elapse of 100 to 700 years between the oldest (Montcineyre) and youngest (Pavin) eruptions (Juvigné and Miallier, 2016). So far, no volcanic eruption in the Massif Central has been dated younger than the Pavin one, nor any unequivocal tephra has been recovered above the Pavin one, so that Pavin currently stands as the youngest volcano in continental France (Juvigné and Miallier, 2016).

Pavin is located only about 40 km South of the southernmost volcano of the Chaîne des Puys, a monogenetic field of about 80 volcanoes, mostly scoria cones, forming a North-South-trending chain about 30 km long, West of the city of Clermont-Ferrand. The Chaîne des Puys volcanoes range in age from less than 100 000 to about 6000-7000 years. The Pavin volcanic group is thus close in age to of the youngest volcanoes of the Chaîne des Puys. Both monogenetic fields occur in the same tectonic setting, in which eruptive vents location is mainly controlled by regional faults dating from the Variscan orogeny and rejuvenated during the post-Alpine rifting episode. In those respects, the Pavin group could be viewed as a southern extension of the larger Chaîne des Puys volcanic field (Boivin et al., 2009).

The Pavin proximal pyroclastic deposits (Camus et al., 1973; Bourdier, 1980; Boivin et al., 2010; Leyrit et al., 2016) have juvenile components consisting of dominant macroscopically homogeneous, yellowish-weathering pumices, and subordinate greyish, denser clasts and texturally heterogeneous pumices (Arbaret and Bourdier, 2018). All textural types are distinctively amphibole-phyric and display similar mineralogy and bulk-rock composition (Bourdier, 1980; Villemant et al., 2016). The juvenile magma is a mildly alkaline (peralkalinity index, P.I. = 0.6-0.8) trachyandesite (or benmoreite) (~58 wt% SiO_2; Table 1, Fig. 2). In the Pavin group, the Montcineyre and Estivadoux magmas are nepheline-normative alkaline basalts to basanites and the Montchal one is a trachybasalt (or hawaiite). Thus, the Pavin magma is the most differentiated (Bourdier, 1980). Previous petrological and geochemical studies have linked the magma compositions of the Pavin group as a differentiation trend dominated by crystal fractionation (Bourdier, 1980; Villemant et al., 2016). In this respect, the Pavin magmatic suite might be compared to the Chaîne des Puys series, this latter being

compositionally more extensive since it shows silica-oversaturated trachytes. The Chaîne des Puys has been consistently modelled as resulting dominantly from crystal fractionation processes in crustal reservoirs (Maury et al., 1980; Villemant et al., 1981), in agreement with petrological and experimental constraints suggesting storage of the Chaîne des Puys trachytes at depths around 10 km (Martel et al., 2013). Recent geochemical modelling of the Pavin suite (Villemant et al., 2016) has stressed the petrogenetic similarities between the Chaîne des Puys and Pavin suites, while pointing to some differences in the fractionation paths. The remoteness of the Pavin volcano from the differentiated volcanoes of the Chaîne des Puys and the small magma volumes involved (of the order of 30-40 Mm^3 DRE for the Pavin magma) imply that the Pavin upper reservoir should be discrete and likely of small volume, so that some differences with the Chaîne des Puys differentiation processes are to be anticipated.

3. Results and discussion

3.1. Petrology of the Pavin trachyandesite

3.1.1. Lithology and whole-rock composition. The Pavin trachyandesite exhibits various textures, from dominantly pumice to denser and darker clasts that differ by vesicularity and groundmass microtexture, while their phenocryst assemblage and whole-rock composition do not show significant differences within the limits of our investigations. Major-element whole-rock compositions are given in Table 1 where the Pavin magma composition is compared to a closely analogous composition (Nugère trachyandesite) and a slightly more evolved one (Clierzou trachyte), both from the Chaîne des Puys volcanic field. All rocks show overall similarities, being metaluminous (P.I. in the 0.6-0.9 range) and close to silica saturation in the CIPW norm. The differentiation trend in the Chaîne des Puys has been thoroughly documented and is compositionally marked by a consistent decrease of FeO, MgO, CaO and increase of alkalis with increasing SiO_2 (Camus, 1975 ; Maury et al., 1980 ; Martel et al., 2013). The Nugère (Chaîne des Puys) and Pavin trachyandesites have close contents for most major elements, though the Pavin composition is consistently richer in TiO_2 and K_2O whereas poorer in P_2O_5. In the Chaîne des Puys differentiation trend, the Na_2O/K_2O ratio does not vary from the Nugère to the Clierzou compositions (Table 1) then it tends to decrease with increasing SiO_2 in the trachyte range, through an increase of K_2O at almost constant Na_2O (Martel et al., 2013 and references therein). The compositional differences between the Pavin and Nugère magmas,

notably the K_2O-richer character of the Pavin magma, are sufficient to indicate that the Pavin magma belongs to a specific differentiation trend, i.e. distinct from the Chaîne des Puys one, as also evidenced by comparing trace-element compositions (Villemant et al., 2016).

3.1.2. Phenocryst assemblage and modal proportion. The phenocryst assemblage of the Pavin magma mostly consists of plagioclase, amphibole, clinopyroxene and Fe-Ti oxides (Appendix B). Phenocrysts are found both isolated and as small glomeroporphyritic agglomerates. Apatite is a common accessory phase. Scarce biotite can be found as inclusions in amphibole and isolated microphenocrysts. Modal proportions range from 10 to 23% (recalculated to 7 to 20 wt% crystallinity; Table 2). Such a variability of the phenocryst proportions could result from heterogeneous distribution at sample scale (e.g. due to the tendency of phenocrysts to agglomerate) or might be acquired through crystallisation along the course of the eruption. No attempt has been made in this study to evaluate the variability of magma crystallinity through the Pavin deposit stratigraphy.

To some extent, the phenocryst assemblage of the Pavin trachyandesite can be compared qualitatively to counterparts from the Chaîne des Puys. Although compositionally close to the Pavin sample, the Nugère trachyandesite is almost aphyric. Other trachyandesites in the Chaîne des Puys, although scarce and volumetrically trivial, typically contain as Fe-Mg phenocrysts both amphibole (more or less stable) and stable clinopyroxene, and lack biotite (Maury et al., 1980). Further, the couple clinopyroxene-amphibole is still present in the less differentiated trachytes, Aumone and Clierzou, which also lack biotite (Boivin et al., 2015). In contrast, biotite is a systematic phase in the more differentiated trachytes, either as the single Fe-Mg phase or accompanied by either amphibole or clinopyroxene, not both (Martel et al., 2013 ; Boivin et al., 2015). The Pavin phenocryst assemblage thus compares well with the Chaîne des Puys magmas at comparable levels of differentiation. The rare occurrence of biotite in the Pavin magma, at lower SiO_2 than needed for biotite appearance in the Chaîne des Puys series, might reflect the higher amount of K_2O in the Pavin magma compared to the Chaîne des Puys ones at similar differentiation degree.

3.1.3. Mineralogy. The natural phases were analysed following the method given in Appendix A2 and the compositions are given in Appendix C.

Plagioclase, although frequently fractured, is euhedral with clear rims, and variously zoned with frequent cloudy to sieved core textures. The plagioclase composition spreads from 32 to 58 mol% of anorthite (An32 to An58), with orthoclase content not exceeding 5% (<Or5) and

consistently increasing as An decreases, (Fig. 3a). Plagioclase rims have a restricted compositional range of An35-38 while most of the cores have compositions of An45-62, with the exception of one profile showing a reverse zoning with core composition down to An32. From core to rim, the plagioclases show either smooth An decrease or drastic drops (Fig. 3b). In the Chaîne des Puys for comparison, plagioclases in the trachyandesites are reported as being mostly in the range of andesine (An30-50; Maury et al., 1980). The plagioclases of the less differentiated Chaîne des Puys trachytes are also andesine, in the range An30-42 with a mean composition of An38 (Martel et al., 2013; Boivin et al., 2015).

Amphibole occurs as 1-2 mm long, euhedral and unresorbed phenocrysts with common inclusions of oxides, apatite and biotite (Appendix B2). The amphibole are kaersutites and hastingsites after Leake et al. (1997), showing a rather scattered range in contents of SiO_2 (38.5-40.7 wt%), Al_2O_3 (11.1-13.9 wt%), Al^{IV} (1.9-2.2), TiO_2 (4.1-5.3 wt%), and Mg# (0.61-0.66) (Appendix C2). Amphibole-rich cumulates are common in the Pavin deposit, notably in the upper part of the deposit stratigraphy. The amphibole from the cumulates is mostly kaersutite that plots separately from the amphiboles analysed in the juvenile pyroclasts (Fig. 4). This is good evidence that the latter form a truly phenocrystic population, without any contribution of xenocrysts of cumulative origin. Within the phenocrystic amphibole population, core and rim compositions do not show systematic variations and are close to each other in the limits of our data set. Thus, the compositional scattering of the amphibole phenocrysts is not related to any significant zoning and likely reflects variations in the crystallization conditions (liquid composition and/or intensive parameters) within the magma reservoir. Amphiboles from the low-silica Clierzou trachyte are also compositionally scattered, but commonly show slightly lower contents in A-site cation number, Al^{IV} content, and Mg# (Fig. 4).

The clinopyroxenes in the juvenile pyroclasts are 1-2 mm long, have smoothed more or less resorbed rims, and contain frequent glass inclusions. They are salites with 44-48 mol% wollastonite (Wo44-48) and 34-45 mol% enstatite (En34-45) (Fig.5a), with notable scattering in SiO_2 and Al_2O_3 contents (Fig. 5b; Appendix C3). By comparison, clinopyroxenes from cumulates are mostly less calcic (Wo41-47) and more magnesian (En39-46), and are on average poorer in SiO_2 and richer in Al_2O_3 and TiO_2 (Fig. 5b; Appendix C3). The compositions of the clinopyroxenes from the cumulates are even more scattered than those of the trachyandesite, suggesting large variations in the crystallization conditions. Compared to the Pavin pumice, clinopyroxenes from the Clierzou trachyte are mostly less calcic (Wo41-47) and more magnesian (En39-46; Fig. 5a), and are on average poorer in SiO_2 and richer in Al_2O_3 (Fig. 5b).

Biotite is scarce and contains about 6 wt% TiO_2, 14.5 wt% MgO and 13-14 wt% Al_2O_3, less than 0.4 wt% MnO and F, with Mg# ~0.65 (Fig. 6; Appendix C4). Comparatively, the Clierzou trachyte does not contain biotite. Biotites are only present in the most differentiated trachytes (>65 SiO_2 wt%) in which they are poorer in magnesian (e.g. Mg# ~0.55; Fig. 6) and slightly richer in alumina (14-15 wt% Al_2O_3 in the Vasset trachyte; Martel et al., 2013) than the Pavin biotites.

Fe-Ti oxides are both magnetite-ulvöspinel and ilmenite-hematite solid solutions (Appendix C5). The isolated phenocrysts often show strong textures of exsolution, whereas Fe-Ti oxides found as mineral inclusions in mostly clinopyroxene and amphibole are texturally and compositionally homogeneous. Fe-Ti oxides in amphibole and clinopyroxene do not show systematic compositional differences. Apparently homogeneous isolated phenocrysts show compositions similar to those found as inclusions, i.e. titanomagnetite with 67-78 mol% magnetite (Mt67-78; with 0.8-1.3 wt% MnO, 79-83 wt% FeO, and 7.5-11.5 wt% TiO_2) and ilmenite with 63-68 mol% ilmenite (Ilm63-68; with 0.8-1 wt% MnO, 55-57 wt% FeO, and 36-38 wt% TiO_2). For comparison, the magnetites and ilmenites from the Clierzou trachytes are Mt- and Ilm-richer, respectively (Mt80-90 and Ilm70-90; Martel et al., 2013).

Glass inclusions are frequently trapped in plagioclases and clinopyoxenes, but are mostly devitrified in the former whereas mostly glassy in the latter, so that all analysed glass inclusions were clinopyroxene-hosted, with one in a magnetite. The compositions are trachytic, showing narrow ranges of 64-66 wt% SiO_2 and 11.5-12.5 wt% alkalis (Appendix C6). The microlite-poor matrix glasses of the Pavin pumices have compositions similar to those of the glass inclusions (Fig. 7). The Pavin glasses overall broadly compare with the bulk-rock compositions of the intermediate-silica trachytes of the Chaîne des Puys (Kilian, Vasset, Sarcouy, Puy de Dôme), except for lower Na_2O and higher K_2O contents (both by ~1 wt%; Fig. 7). The K_2O-richer character of the Pavin glasses conforms to the K_2O-richer content of the Pavin whole-rock trachyandesite compared to Chaîne des Puys analogues.

The H_2O contents of the Pavin glasses are inferred from a calibrated by-difference method (see Appendix A2), which assumes that volatiles other than H_2O can be neglected. Fluorine contents are below 0.5 wt% in the Pavin glass inclusions (Appendix C6), in agreement with the fluorine, chlorine, and sulphur contents below 0.5 wt% for the glass inclusions of the Chaîne des Puys trachytes (Martel et al., 2013). We thus assume that H_2O is by far the most abundant volatile species and that the inferred values cannot be overestimated by more than 0.5 wt%. The range of H_2O content is large, with the matrix glasses showing low contents (< 1.5 wt%) and the glass inclusions ranging between 1.1 and 5.3 wt% H_2O (Fig. 8; Appendix C6).

3.2. Crystallization conditions retrieved from the natural samples

3.2.1. Phase assemblage and compositions relevant to the reservoir conditions. The natural pumice pyroclasts contain phenocrysts of plagioclase, amphibole, clinopyroxene, magnetite, ilmenite, and minor apatite. The scarcity of biotite, only found as inclusions in amphibole or rare isolated microphenocrysts, likely reflects inherited crystals.

We selected pumice clasts from an explosive event during which magma was supposed to ascend rapidly from the storage region to the surface. This has the advantage to minimize syn-eruptive crystallization, although the samples do contain some microlites that evidence crystallization after reservoir exit. If such syn-eruptive crystallization is negligible, the pre-eruptive phase compositions are provided by the phenocryst rims in equilibrium with the interstitial glass (or alternatively glass inclusions if they were not compositionally modified after entrapment). The plagioclase phenocrysts show rim compositions of An35-40 (Fig. 3b) that turned out to be impossible to reproduce under realistic storage conditions, as evidenced experimentally below. Rather, the plateau range of An46-52 present in most of the plagioclase phenocrysts seems to represent the pre-eruptive compositions, whereas compositions <An40 may reflect crystallization stages at shallower levels. Contrary to plagioclase, the other phenocrysts do not show significant compositional zonings, possibly reflecting their slower crystallization kinetics or lower compositional sensitivity to (lower) pressure and melt H_2O content. The crystallization of plagioclase rims and microlites after reservoir exit lead to residual liquids more differentiated (silica-richer) than those in equilibrium in the reservoir. In contrast, melt trapped as inclusions by phenocrysts growing in the reservoir may be more representative of the pre-eruptive melt composition. Yet, microlite-bearing residual glasses and glass inclusions globally cover the same compositional range (Fig. 7), suggesting a similar compositional evolution. In particular, the Fe-Mg partition coefficients between glass inclusion and host clinopyroxene give a mean value of $0.11_{\pm 0.03}$, whereas reaching $0.25_{\pm 0.04}$ for the experimental melt-clinopyroxene pairs (in agreement with the $0.28_{\pm 0.09}$ given by Putirka, 2008), which likely suggests some compositional modification of the melt inclusions after entrapment.

Therefore, the experiments should reproduce 7-20 wt% phenocrysts consisting of $An49_{\pm 3}$ plagioclase, amphibole with $12_{\pm 1}$ wt% Al_2O_3 ($Am12_{\pm 1}$), $Wo46_{\pm 2}$ clinopyroxene, $Mt72_{\pm 5}$ magnetite, $Ilm65_{\pm 2}$ ilmenite, and apatite in a glass with less than $65_{\pm 1}$ wt% SiO_2 and up to 5.5 wt% H_2O as shown by the glass inclusions (keeping in mind though that they were mostly modified after entrapment).

3.2.2. Intensive parameters inferred from the natural assemblage. Pairs of coexisting Mt and Ilm, either trapped in phenocrysts (clinopyroxene or amphibole) or as individual phenocrysts, can be used to constrain the temperature (T) and oxygen fugacity (fO_2) prevailing at the time of their crystallization, provided they co-crystallized from the same parental melt. Pairs that were positively tested for chemical equilibrium (after Bacon & Hirschmann, 1988) were used to calculate T-fO_2 values following the formulation of Sauerzapft et al. (2008). Since this formulation is not calibrated originally for trachyandesitic to trachytic compositions, we tested it against the experimental oxides that crystallized under controlled T and fO_2. The results give T estimates up to 40 °C and fO_2 up to 1.3 log units, but mostly agree within 0.3 log units with the experimental conditions (Appendix D1), so that we validated the method for the Pavin compositions. The calculations on the natural Mt-Ilm pairs give T between 850 and 970 °C and fO_2 in the range of NNO+1.3 to +1.9.

No thermodynamic model is adequately calibrated to estimate total pressure (P) for trachyandesite compositions and phase assemblages such as the Pavin ones. Nevertheless, the formulations of Ridolfi & Renzulli (2012), based on amphibole composition, were tested. Compared to the run P, the calculations give significant and systematic P overestimations by over 100 MPa (e.g. 105 to $304_{\pm 50}$ MPa; Appendix D2). Such calculations also overestimate T by 41 to 146 °C, whereas underestimating fO_2 by about 1 log unit (Appendix D2). Therefore, we cannot consider the formulations of Ridolfi & Renzulli (2012) relevant for amphiboles crystallizing from the Pavin trachyandesite.

The pre-eruptive H_2O content may be inferred from H_2O dissolved in glass inclusions, assuming volatile tightness after reservoir exit. Although the large variability in H_2O contents (1.1-5.3 wt%; Fig. 8) likely suggests that not all glass inclusions remained sealed after reservoir exit, the H_2O-richer ones suggest entrapment pressures of ~120 MPa (Di Matteo et al., 2004; minimum value if not H_2O saturated).

3.3. Experimentally-determined storage conditions of the Pavin trachyandesite

In order to better constrain the storage conditions, phase-equilibrium experiments starting from the fused Pavin trachyandesite were performed following the method given in Appendix A1. The experimental conditions were chosen to cover the range of intensive parameters inferred from the natural assemblage. Therefore, crystallization experiments were performed

from 850 to 950 °C, 150 to 400 MPa, NNO to NNO+2, and X_{H2Oin} ranging from 0.7 to 1 (i.e. melt H_2O contents from 4.5 to 9.5 wt%; Table 3). Below, we compare the natural phase assemblage, proportion, and compositions to those obtained experimentally (Fig. 9, with phase relationships and compositions described in Appendix E).

At ~400 MPa and NNO+1.5, stable plagioclase, amphibole, and clinopyroxene require H_2O contents around 8 wt% and *T* close to 900 °C (Fig. 9c). Yet, the crystallinities of the run products at these conditions are much higher (~70 wt%) than those of the Pavin samples (11-20 wt%), biotite is ubiquitous although not considered as stable in the reservoir, and the experimental glass compositions are systematically off the trend defined by the Pavin whole-rock and natural glasses in CaO, Al_2O_3, and alkali contents (Fig. 7). Varying *T* from 850 to 1000 °C would not help reconciling these discrepancies, since biotite would still be present, amphibole and clinopyroxene would not coexist, and/or the modal proportions would be too low (Fig. 9). Therefore, 400 MPa is not a realistic *P* for storing the Pavin magma.

Similarly, at ~300 MPa and NNO+1, plagioclase, amphibole, and clinopyroxene are stable at *T*-H_2O conditions for which crystallinities are $\geq$ 40 wt%, biotite is present (Fig. 9b), and the residual glasses hardly agree with the trend defined by the Pavin whole-rock and natural glasses (Fig. 7). Therefore, it rules out 300 MPa as a possible storage *P* for the Pavin reservoir.

At 150-200 MPa, ~NNO+1, and 950 to 975 °C, H_2O saturation conditions (7.0 wt% H_2O) do not allow clinopyroxene crystallization. Even if slightly more oxidized conditions could compensate for this, the plagioclase An content would be significantly higher than An52 (Fig. 9a). Similarly, for lower H_2O contents of ~6 wt%, the plagioclase An content is between 51 and 57 wt% (Fig. 9b). For H_2O contents between 4.5 and 5.5 wt%, however, ~An50 crystallizes, together with Wo44-47 and Am11-12 (Fig. 9c). the Fe-Ti oxide compositions, Mt60-61 and Ilm84-87, likely suggest too low f_{O2} conditions compared to the natural Fe-Ti oxides ($Mt72_{\pm5}$ and $Ilm65_{\pm2}$). In view of the Mt84 that crystallized together with hematite at NNO+2, it is reasonable to predict that a f_{O2} intermediate between NNO+1 and +2 would allow Fe-Ti oxide compositions close to the natural ones. This is in agreement with the natural Mt-Ilm pairs suggesting NNO+1.3 to +1.9 for *T* between 850 and 970 °C. The 15-22 wt% crystallinity at 975 °C for H_2O contents of 4.5-5.5 wt% is compatible with the natural crystallinities (7-20 wt%), but the residual liquid contains ~62 wt% SiO_2, i.e. significantly less than for the natural glasses (64-66 wt% SiO_2). Vice versa, experimental liquids with 64 wt% SiO_2 result from crystallinities much higher than expected from the natural samples (e.g. 76 wt% crystals, including 36 wt% plagioclase, at 950 °C, ~5.5 wt% H_2O, and NNO+2). Yet, the natural residual liquids

crystallized and differentiated during ascent in the conduit, thus not excluding liquids with 62 wt% SiO_2 as possible pre-eruption compositions.

In summary, the storage conditions for the Pavin trachyandesite could be close to 150-200 MPa (~5.5-7.0 km in depth), 950-975 °C, NNO+1.5, and melt H_2O content about 4.5-5.5 wt% (Fig. 10). Noteworthy, these *P*-*T* conditions are outside, but close to the stability field of biotite, and inside, but close to clinopyroxene destabilization, which may in both cases accounts for their presence but low abundance in the natural samples.

3.4. Reservoir and eruption dynamics

The Pavin juvenile products provide petrological information on (1) the reservoir dynamics prior to eruption, and (2) the eruptive conditions upon ascent of the magma towards surface.

3.4.1 Reservoir dynamics. The juvenile pumice shows a great variability in many petrological features as shown above, notably phenocryst proportions, amphibole and clinopyroxene compositional scatter, and plagioclase zonings. Such heterogeneities likely points to variability in the differentiation process, in terms of liquid-crystal ratio and intensive parameters. This is further demonstrated by the inability of any of our phase-equilibrium experiments to fulfill the observed natural assemblage and phase compositions. Actually, the inferred intensive parameters can only be bracketed, the somewhat limited range of parameters fixed above representing the conditions for the mean assemblage and compositions. Indeed, the delimited *P*-*T* field for the Pavin storage conditions is tightly bordered by the clinopyroxene, ilmenite, and biotite appearance curves, so that slight *P*-*T*-f_{O2} variations may drastically modify the phase assemblage and the liquid-crystal ratio (e.g. decreasing *T* to 950 °C leads to biotite crystallization and total crystallinities of ~70 wt%; Fig. 9c).

The Pavin volcano is an isolated monogenetic crater of trachyandesitic composition, suggesting it is fed by a short-lived reservoir of likely small volume. Small polycrystalline cumulates and free cumulative crystals are abundant in the uppermost part ash fraction of the pyroclastic sequence, suggesting that the eruption tapped lower cumulative parts of the reservoir. This highlights that the reservoir was likely emptied and thus of small volume. We argue that the observed variability in phase compositions is well explainable if considering a small volume reservoir where magma evolves under strong gradients of physical parameters (notably temperature that in turn controls phase assemblage and magma crystallinity). In this respect, the Pavin case contrasts with many documented large volume silicic eruptions, notably

ignimbritic ones, where phase assemblage and compositions are more homogeneous, likely resulting from the buffering effect of large magma volume on the controlling physico-chemical parameters.

3.4.2. Conduit dynamics. The incompatibility between the plagioclase rim compositions of An32-40 (Fig. 3b) and the experimental compositions in the 150-400 pressure range (Fig. 9) argues for plagioclase crystallization upper in the conduit. Some of the plagioclase rims show a gradual An decrease, whereas others show a drastic drop (Fig. 3b), suggesting that the magma may have reached this intermediate storage level following different ascent rates. Similarly, some clinopyroxene-hosted melt inclusions preserved the pre-eruptive melt H_2O contents of ~4.5-5.5 wt%, whereas most of them are H_2O poorer (Fig. 8), likely reflecting imperfect tightness and connection with the residual liquid during magma ascent (Humphreys et al., 2008). Most of the glass inclusions contain ~3 wt% H_2O, suggesting quench pressures around 50 MPa (Di Matteo et al., 2004). Such a melt inclusion re-equilibration pressure is compatible with crystallization of An32-40 plagioclase. Therefore, we assume that parts of the magma crystallized at an intermediate level of ~50 MPa (i.e. 2.0 km depth), whereas other batches ascended fast enough to preserve the pre-eruptive phase compositions and H_2O contents. The 0.3 to 1.2 wt% H_2O of the residual glasses mark a later degassing that is not associated with crystallization, probably due to the slow kinetics and large crystal nucleation delays prevailing at low pressures (Mollard et al., 2012). The residual glass H_2O contents below 1.2 wt% reflect pumice clast quenching at fragmentation depth below 1 km ($P \leq 20$ MPa; Fig. 10).

3.5. Differentiation trend and comparison with the volcanic suite of the Chaîne des Puys

Plotted in Harker diagrams, the experimental residual glasses show major compositional differences with pressure, i.e. the 150-200 MPa glasses are trachyandesitic to trachytic (alkaline trend) whereas the 300-400 MPa glasses are dacitic to rhyolitic in terms of silica and alkali contents (sub-alkaline trend; Fig. 7). In details, the compositional differences in the residual glasses from both pressure series come from major differences in the crystallized mineral assemblage and proportion, as demonstrated for basalts in the pioneer work by Grove and Baker (1984). This is highlighted by the total silica content of the crystallized minerals, which is ~50 wt% SiO_2 in the 150-200 MPa charges, whereas ~40 wt% in the 300-400 MPa samples (Table 3). Early fractionation of plagioclase and amphibole has already been recognized as a key process in generating alkaline liquids (Villemant et al., 2016), but the quasi ubiquity of both

phases in the experimental products does not allow deciphering the residual glass composition. Yet, biotite (low-silica phase) seems to be a major component driving the residual liquids towards high-silica low-alkali contents (sub-alkaline trend), whereas biotite-absent products show residual liquids following the alkaline trend. The lack of biotite in the Pavin magma may result from crystallization at low pressure (150-200 MPa), but also from relatively oxidized conditions (NNO+1.5) that favour clinopyroxene at the expense of biotite (Fig. 9a). Therefore, the pressure-driven crystallization sequence of a trachyandesitic melt deciphers the liquid line of descent, with major implications for alkaline versus sub-alkaline volcanic suites. Typically, the low-pressure biotite-lacking Pavin magma has a trachytic residual liquid, but it could have been different in case of crystallization at deeper levels in the stability field of biotite.

The trachytic residual liquid of the Pavin magma overlaps in major oxides with the trachytic whole-rocks of the neighbouring Chaîne des Puys (Fig. 7; except that the Pavin glasses are enriched by ~1 wt% K_2O and depleted by ~1 wt% Na_2O compared to those of the Chaîne des Puys, which has been attributed to preferential fractionation of amphibole at the expense of clinopyroxene; Villemant et al., 2016). However, the accordance of the other oxides (and total alkali) makes it possible the generation of trachytic liquids by main fractionation of amphibole, plagioclase, and clinopyroxene from a trachyandesitic parent at upper crustal conditions (< 10 km), in agreement with previous mineralogical and geochemical studies on the Massif Central magmatic suites (e.g. Maury et al., 1980 ; Villemant et al., 1981). The trachyandesitic melts (such as the ones of the Pavin or Nugère for the Chaîne des Puys) may have fractionated early amphibole and plagioclase at upper crust level, but our experimental results bring the additional constraint that they did not fractionate significant biotite to produce trachytic residual liquids.

4. Conclusion

The Pavin pyroclasts are relatively heterogeneous in composition (crystal zonings, glomerocrysts, cumulates, etc…), which may result from two main processes: (i) a small volume of stored magma that makes it significantly sensitive to any physico-chemical changes induced by deep magma recharge and (ii) an intermediate magma storage within the conduit (up to ~50 MPa; ~2.0 km deep) that promotes crystallization of microlites, microphenocrysts, and phenocryst rims. Evaluating the phase assemblage and compositions that prevail in the reservoir, we infer magma storage conditions around 950-975 °C, 150-200 MPa (~5.5-7.0 km in depth), NNO+1.5, and 4.5-5.5 wt% melt H_2O. The residual liquids in equilibrium at these

conditions are trachytic and compare to those of the neighbouring Chaîne des Puys trachytes (whole-rock), making it possible a differentiation trend by fractionation of at least 10-20 wt% of amphibole, plagioclase, and clinopyroxene. The experiments highlight the importance of crystallizing this assemblage at 150-200 MPa and out of the stability field of biotite to produce the trachytic liquids. In contrast, biotite plays a major role at 300-400 MPa in driving liquids towards sub-alkaline trends.

Acknowledgements

We thank Ida Di Carlo for assistance with SEM and EMP analyses, Rémi Champallier for assistance with the IHPV, and Michel Pichavant for fruitful discussions. This work is part of MR's undergraduate research project which was partly funded by TLS Geothermics (France) and the french Investissements d'Avenir program Equipex_Planex (ANR-11-EQPX-0036; B. Scaillet). We greatly thank the reviewers for their useful suggestions that improved the manuscript.

References

Ackerman, L., Ulrych, J., Řanda, Z., Erban, V., Hegner, E., Magna, T., Balogh, K., Frána, J., Lang, M., Novák J., 2015. Geochemical characteristics and petrogenesis of phonolites and trachytic rocks from the České Středohoří Volcanic Complex, the Ohře Rift, Bohemian Massif. Lithos 224-225, 256-271.

Arbaret, L., Bourdier, J.-L., 2018. Assessing the role of phreatomagmatism in the eruption dynamics of the trachyandesitic maar-like Pavin crater (Massif central, France): constraints from the pyroclasts microtextures. 7th International Maar Conference, Olot, Spain, Abst. Vol. p. 18-19.

Bacon, C.R., Hirschmann, M.M., 1988. Mg/Mn partitioning as a test for equilibrium between coexisting Fe-Ti oxides. Am. Mineral. 73, 57-61.

Boivin, P., Besson, J.-C., Briot, D., Camus, G., de Goër de Herve, A., Gourgaud, A., Labazuy, P., Langlois, E.P., de Larouzière, F.D., Livet, M., Mergoil, J., Miallier, D., Morel, J.M., Vernet, G., Vincent, P., 2009. Volcanologie de la Chaîne des Puys. Parc Naturel Régional de la Chaîne des Puys (Ed.), Carte et fascicule, 5e ed., 200 p.

Boivin, P., Besson, J.-C., Ferry, P., Gourgaud, A., Miallier, D., Thouret, J.-C., Vernet, G., 2010. Le point sur l'éruption du lac Pavin il y a 7 000 ans. Rev. Sci. Nat. Auv. 74-75, 45-56.

Boivin, P., Miallier, D., Cluzel, N., Devidal, J.-L., Dousteyssier, B., 2015. Building and ornamental use of trachyte in the center of France during antiquity: Sources and criteria of identification. J. Archaeol. Sci. 3, 247-256.

Bourdier, J.-L., 1980. Contribution à l'étude volcanologique de deux secteurs d'intérêt géothermique dans le Mont Dore : le group du Pavin et le Massif du Sancy. PhD thesis, Univ. Clermont-Ferrand II, 180 p.

Briot, D., Cantagrel, J.-M., Dupuy, C., Harmon R.S., 1991. Geochemical evolution in crustal magma reservoirs: Trace-element and Sr-Nd-O isotopic variations in two continental intraplate series at Monts Dore, Massif Central, France. Chem. Geol. 89, 281-303.

Brousse, R., 1961. Minéralogie et pétrologie des roches volcaniques du Massif du Mont Dore. Bull. Soc. Fr. Minéral. Cristallogr. 84, 131-186, 245-259.

Camus, G., 1975. La Chaîne des Puys (Massif Central Français): Etude structurale et volcanologique. PhD thesis, Univ. Clermont-Ferrand II, France.

Camus G., Goër de Herve A., Kieffer G., Mergoil J., Vincent P.M., 1973. Mise au point sur le dynamisme et la chronologie des volcans holocènes de la région de Besse-en-Chandesse (Massif Central français). C. R. Acad. Sci. Paris, série D 277, 629-632.

Di Matteo, V., Carroll, M. R., Behrens, H., Vetere, F., Brooker, R. A., 2004. Water solubility in trachytic melts. Chem. Geol. 213, 187-196.

Downes, H., 1984. Sr and Nd isotope geochemistry of coexisting alkaline magma series, Cantal, France. Earth Planet. Sci. Lett. 69, 321-334.

Downes, H., 1987. Tertiary and Quaternary volcanism in the Massif Central, France. In: Fitton, J.C, Upton, B.G. (Eds.), Alkaline igneous rocks, Geol. Soc. Spec. Publ. 30, 517-530.

Grove, T.L., Baker, M.B., 1984. Phase equilibrium controls on the tholeiitic versus calc-alkaline differentiation trends. J. Geophys. Res. 89, B5, 3253-3274.

Humphreys, M.C.S., Menand, T., Blundy, J.D., Klimm, K., 2008. Magma ascent rates in explosive eruptions: constraints from H_2O diffusion in melt inclusions. Earth Planet. Sci. Lett. 270, 25-40.

Juvigné, E., Miallier, D., 2016. Distribution, tephrostratigraphy and chronostratigraphy of the widespread eruptive products of Pavin volcano. In: Sime-Ngando, T., Boivin, P., Chapron, E., Jézéquel, D, Meybeck, M. (Eds), Lake Pavin, Springer Int. Publ., Switzerland, pp. 143-154.

Leake, B.E., Woolley, A.R. Arps, C.E.S., Birch, W.D., Gilbert, C.M., Grice, J.D., Hawthorne, F.C., Kato, A., Kisch, H.J., Krivovichev, V.G., Linthout, K., Laird, J., Mandarino, J.A., Maresch, W.V., Nickel, E.H., Rock, N.M.S., Schumacher, J.C., Smith, D.C., Stephenson,

N.C.N., Ungaretti, L., Whittaker, E.J.W., Youzhi., G., 1997. Nomenclature of amphiboles: Report of the subcommittee on amphiboles of the International Mineralogical Association, Commission on New Minerals and Mineral Names. Can. Mineral. 35, 219-246.

Le Bas, M.J., Le Maître, R.W., Streckeisen, A., Zanettin B., 1986. A chemical classification of volcanic rocks based on the total alkali-silica diagram. J. Petrol. 27, 745-750.

Leyrit, H., Zylberman, W., Lutz, P., Jaillard, A., Lavina, P., 2016. Characterization of phreatomagmatic deposits from the eruption of the Pavin maar (France). In: Sime-Ngando, T., Boivin, P., Chapron, E., Jézéquel, D, Meybeck, M. (Eds), Lake Pavin, Springer Int. Publ., Switzerland, pp. 105-128.

Lustrino, M., Wilson, M., 2007. The circum-Mediterranean anorogenic Cenozoic igneous province. Earth Sci. Rev. 81(1), 1-65.

Martel, C., Champallier, R., Prouteau, G., Pichavant, M., Arbaret, L., Balcone-Boissard, H., Boudon, G., Boivin, P., Bourdier, J.-L., Scaillet, B., 2013. Phase relations in trachytes and implication for magma storage conditions in the Chaîne des Puys (French Massif Central). J. Petrol. 54(6), 1071-1107.

Maury, R., Brousse, R., Villemant, B., Joron, J.-L., Jaffrezic, H., Treuil, M., 1980. Cristallisation fractionnée d'un magma basaltique alcalin: la série de la Chaîne des Puys (Massif Central, France). I. Pétrologie. Bull. Minéral. 103, 250-266.

Mollard, E., Martel, C., Bourdier, J.-L., 2012. Decompression-induced crystallization in hydrated silica-rich melts: Empirical models of experimental plagioclase nucleation and growth kinetics. J. Petrol. 53(8), 1743-1766.

Putirka, K.D., 2008. Thermometers and barometers for volcanic systems. Rev. Mineral. Geochem. 69(1), 61-120.

Ridolfi, F., Renzulli, A., 2012. Calcic amphiboles in calc-alkaline and alkaline magmas: thermobarometric and chemometric empirical equations valid up to 1,130° C and 2.2 GPa. Contrib. Mineral. Petrol. 163(5), 877-895.

Sauerzapf, U., Lattard, D., Burchard, M., Engelmann, R., 2008. The titanomagnetite–ilmenite equilibrium: new experimental data and thermo-oxybarometric application to the crystallization of basic to intermediate rocks. J. Petrol. 49(6), 1161-1185.

Schreiber, U., Anders, D., Koppen, J., 1999. Mixing and chemical interdiffusion of trachytic and latitic magma in a subvolcanic complex of the Tertiary Westerwald (Germany). Lithos 46(4), 695-714.

Ulrych, J., Pivec, E., Lang, M., Balogh, K., Kropáček, V., 1999. Cenozoic intraplate volcanic rock series of the Bohemian Massif: a review. Geolines 9, 123–129.

Villemant, B., 1979. Etude géochimique des éléments en traces dans les séries volcaniques du Massif Central. PhD Thesis, Univ. Paris, 347 p.

Villemant, B., Jaffrezic, H., Joron, J.-L., Treuil, M., 1981. Distribution coefficients of major and trace elements, fractional crystallization in the alkali basalts of Chaine des Puys (Massif Central, France). Geochim. Cosmochim. Acta 45, 1997-2022.

Villemant, B., Joron, J.-L., Jaffrezic, H., Treuil, M., Maury, R., Brousse, R., 1980. Cristallisation fractionnée d'un magma basaltique alcalin: la série de la Chaîne des Puys (Massif Central, France). II. Géochimie. Bull. Minéral. 103, 267-286.

Villemant, B., Caron, B., Thierry, P., Boivin, P., 2016. Magmatic evolution of Pavin's group of volcanoes: petrology, geochemistry and modeling of differentiation processes. In: Sime-Ngando, T., Boivin, P., Chapron, E., Jézéquel, D, Meybeck, M. (Eds), Lake Pavin, Springer Int. Publ., Switzerland, pp. 129-140.

Wilson, M., Downes, H., Cebria J.-M., 1995. Contrasting fractionation trends in coexisting continental alkaline magmas series; Cantal, Massif Central, France. J. Petrol. 36, 1729-1753.

Wörner, G., Beusen, J.M., Duchateau, N., Gijbels, R., Schmincke, H.U., 1983. Trace element abundances and mineral/melt distribution coefficients in phonolites from Laacher See Volcano (Germany). Contrib. Mineral. Petrol. 84, 152-173.

Figure captions

Figure 1. Localization of the Pavin group (modified after Bourdier, 1980), Pavin group simplified stratigraphic sequence (modified after Boivin et al., 2009), and the Pavin volcano stratigraphic sequence at Clidères outcroup showing the fallout level (basis of B2) where pumices have been sampled for the experiments.

Figure 2. Total alkalis versus SiO_2 bulk-rock compositions of the magmas from the Pavin-group (in green) and the Chaîne des Puys (CDP; in red), as given in Table 1 (recalculated without P_2O_5 and total iron as FeO) and in Martel et al. (2013) for the CDP trachytes; Volcanic rock classification after Le Bas et al. (1986).

Figure 3. **a.** Natural and experimental plagioclase compositions recalculated as anorthite (An), albite (Ab), and orthoclase (Or) mol%, as given in Appendix C1 and **b.** Analytical profiles from rim to core, with the yellow box showing the An_{45-50} plateau value present in nearly all plagioclases and interpreted as the pre-eruptive compositions in the reservoir (see text). Higher An content may be inherited cores from the Montchal trachybasalt (as suggested by the

Montchal plagioclase composition in **a)**. The red box shows the An_{35-40} rim composition present in all phenocrysts that may reflect a shallow level of crystallization (see text).

Figure 4. Natural and experimental amphibole compositions recalculated as Al^{IV} content versus **a.** cations in A-site (pfu) and **b.** Mg#, as given in Appendix C2.

Figure 5. Natural and experimental clinopyroxene compositions recalculated as **a.** enstatite (En), wollastonite (Wo), ferrosilite (Fs) mol% and **b.** Al_2O_3 versus SiO_2 wt%, as given in Appendix C3.

Figure 6. Natural and experimental biotite compositions recalculated as Mg# versus SiO_2 wt%, as given in Appendix C4.

Figure 7. Natural and experimental glass compositions plotted in Harker diagrams, as given in Appendix C6 (glasses are corrected for Na_2O and normalized to 100 wt% on a volatile-free basis).

Figure 8. Melt H_2O content of glass inclusions (*circles*; clinopyroxene- or magnetite-hosted) and matrix glasses (*squares*) as given in Appendix C6.

Figure 9. Pressure-temperature phase stability of the Pavin trachyandesite as a function of H_2O content: **a.** X_{H2Oin}=1 (H_2O saturation), **b.** X_{H2Oin}~0.8, and **c.** X_{H2Oin}~0.7 (black and green circles for NNO+1 and NNO+2, respectively). The right Y-axes give melt H_2O content calculated after *equation* 1 in Appendix A2. The point labels give the crystallinity in wt% (in bracket) followed by the phase compositions : plagioclase as anorthite mol% (An), amphibole (Am) as Al_2O_3 wt%, clinopyroxene as wollastonite mol% (Wo), biotite as Mg#, titanomagnetite as magnetite mol% (Mt), and glass as liquid (Liq) SiO_2 wt% (all compositions given in Appendix C). The crystallinity (void-free basis) and phase compositions of the natural pumice samples are given in figure title. The dashed red circle shows the experimental conditions that best reproduce the natural phase assemblage and compositions.

Figure 10. Schematic view of the plumbing system beneath the Pavin volcano showing the magma storage conditions and the eruptive scenario based on petrological information. Phase abbreviations and composition as in Fig. 9. See text for explanations.

Figure 1

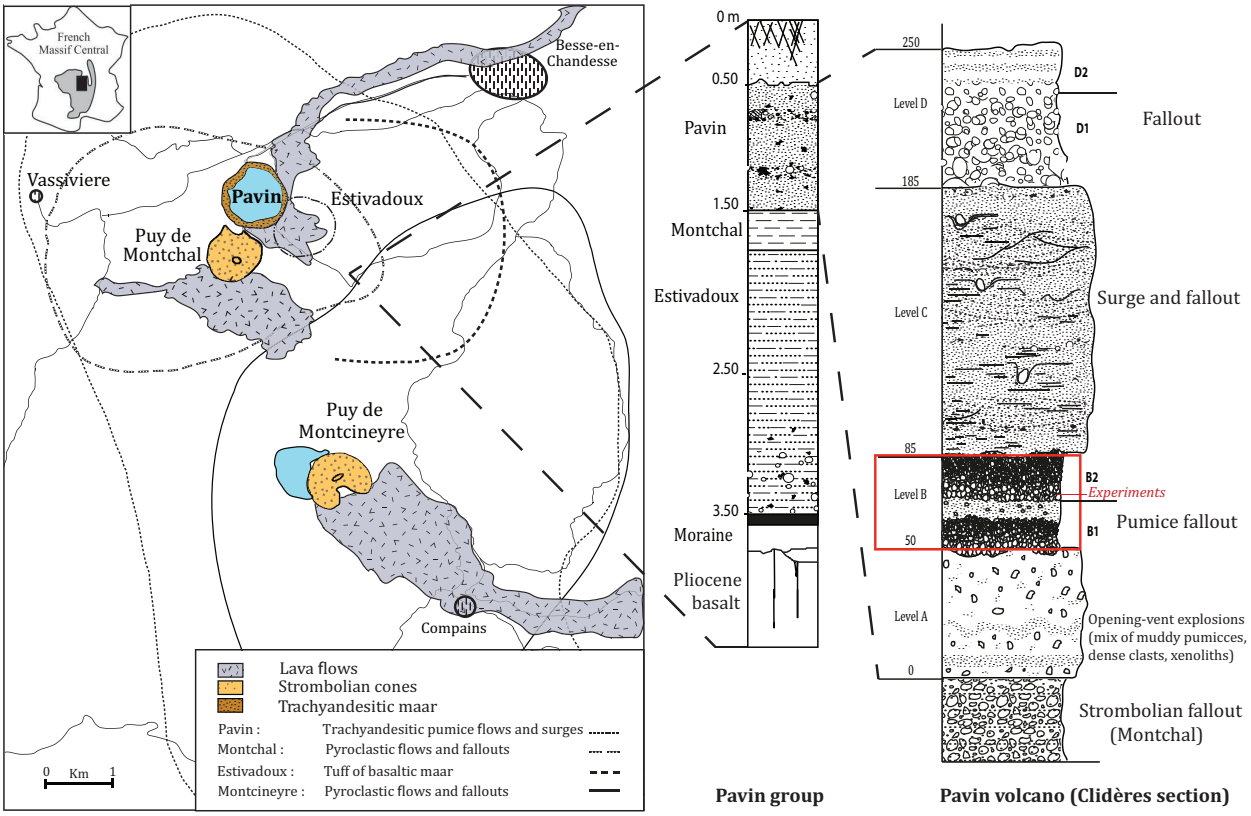
French Massif Central
Besse-en-Chandesse
Vassiviere
Pavin
Estivadoux
Puy de Montchal
Puy de Montcineyre
Compains
0 Km 1
Lava flows
Strombolian cones
Trachyandesitic maar
Pavin : Trachyandesitic pumice flows and surges
Montchal : Pyroclastic flows and fallouts
Estivadoux : Tuff of basaltic maar
Montcineyre : Pyroclastic flows and fallouts
0 m
0.50
Pavin
1.50
Montchal
Estivadoux
2.50
3.50
Moraine
Pliocene basalt
Pavin group
250
Level D
D2
D1
Fallout
185
Level C
Surge and fallout
85
Level B
B2
Experiments
Pumice fallout
B1
50
Level A
Opening-vent explosions (mix of muddy pumicces, dense clasts, xenoliths)
0
Strombolian fallout (Montchal)
Pavin volcano (Clidères section)

Figure 2

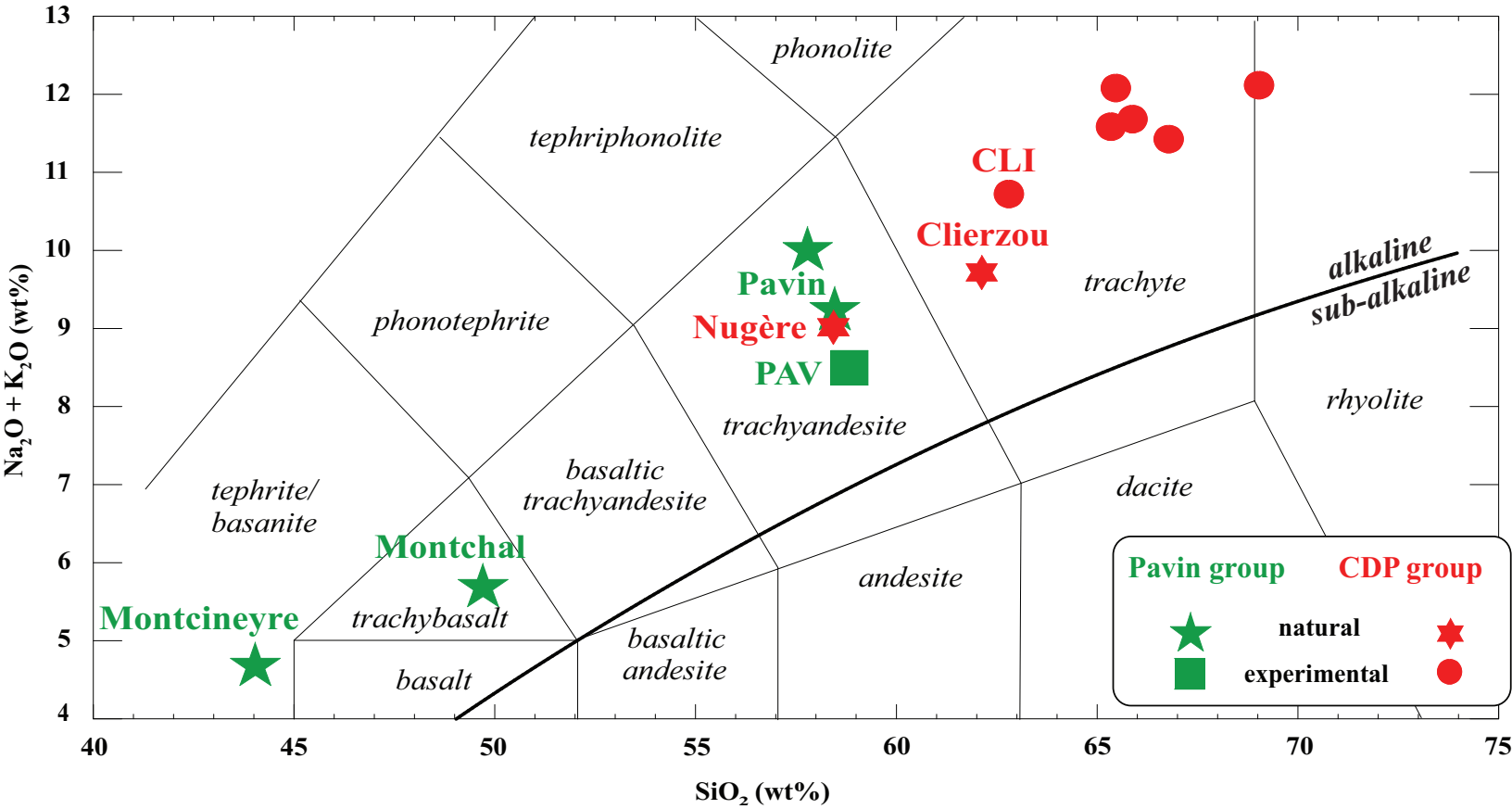
phonolite
tephriphonolite
phonotephrite
tephrite/
basanite
basaltic
trachyandesite
trachyandesite
trachyte
dacite
rhyolite
andesite
basaltic
andesite
trachybasalt
basalt
alkaline
sub-alkaline
CLI
Clierzou
Pavin
Nugère
PAV
Montchal
Montcineyre
Pavin group
CDP group
natural
experimental
Na2O + K2O (wt%)
SiO2 (wt%)
13
12
11
10
9
8
7
6
5
4
40
45
50
55
60
65
70
75

Figure 3

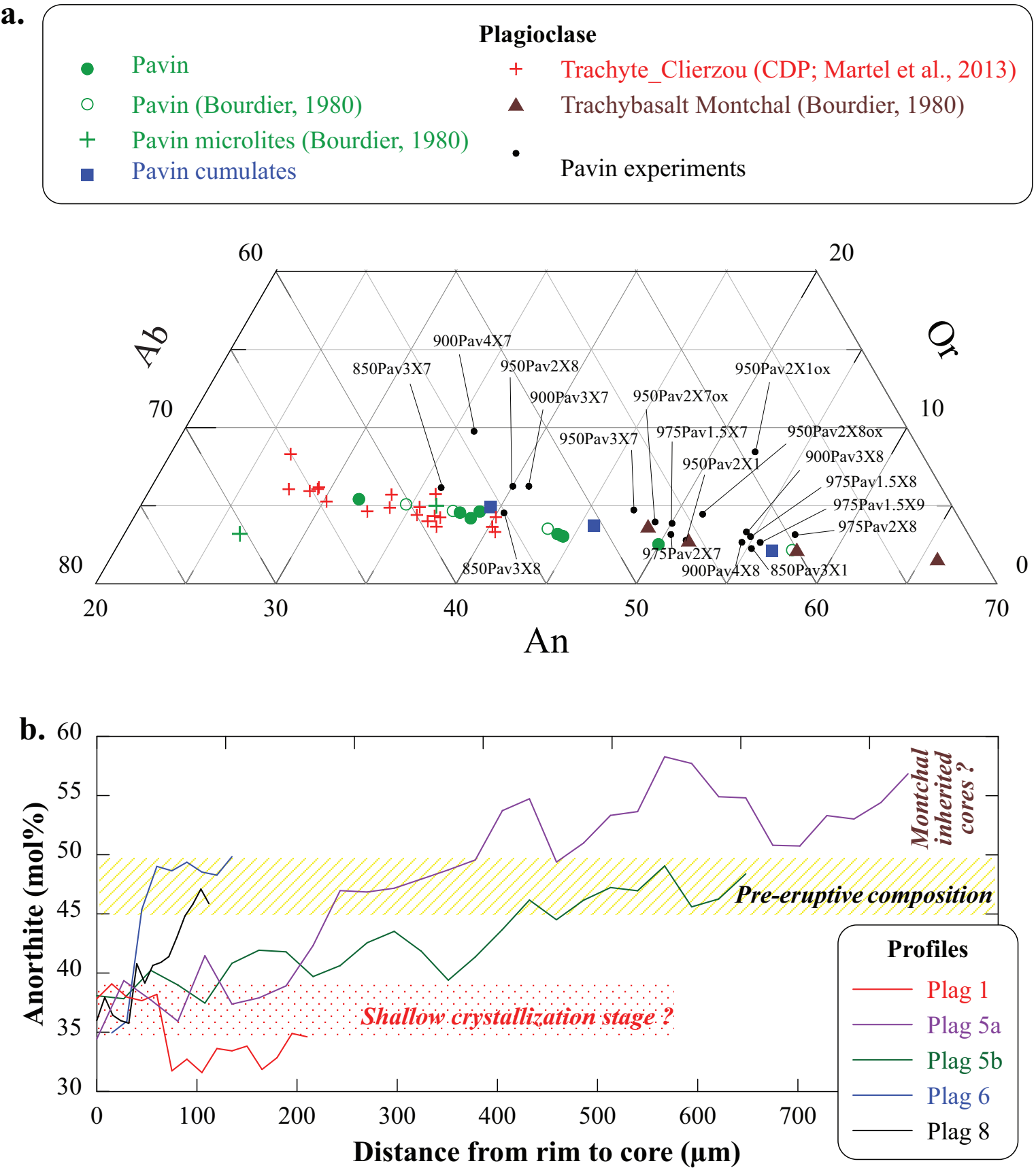
a.
Plagioclase
Pavin
Pavin (Bourdier, 1980)
Pavin microlites (Bourdier, 1980)
Pavin cumulates
Trachyte_Clierzou (CDP; Martel et al., 2013)
Trachybasalt Montchal (Bourdier, 1980)
Pavin experiments
Ab
Or
An
60
20
70
10
80
0
20
30
40
50
60
70
900Pav4X7
850Pav3X7
950Pav2X8
900Pav3X7
950Pav2X7ox
950Pav2X1ox
950Pav3X7
975Pav1.5X7
950Pav2X8ox
950Pav2X1
900Pav3X8
975Pav1.5X8
975Pav1.5X9
975Pav2X8
975Pav2X7
900Pav4X8
850Pav3X1
850Pav3X8
b.
Anorthite (mol%)
60
55
50
45
40
35
30
0
100
200
300
400
500
600
700
Distance from rim to core (µm)
Montchal inherited cores ?
Pre-eruptive composition
Shallow crystallization stage ?
Profiles
Plag 1
Plag 5a
Plag 5b
Plag 6
Plag 8

Figure 4

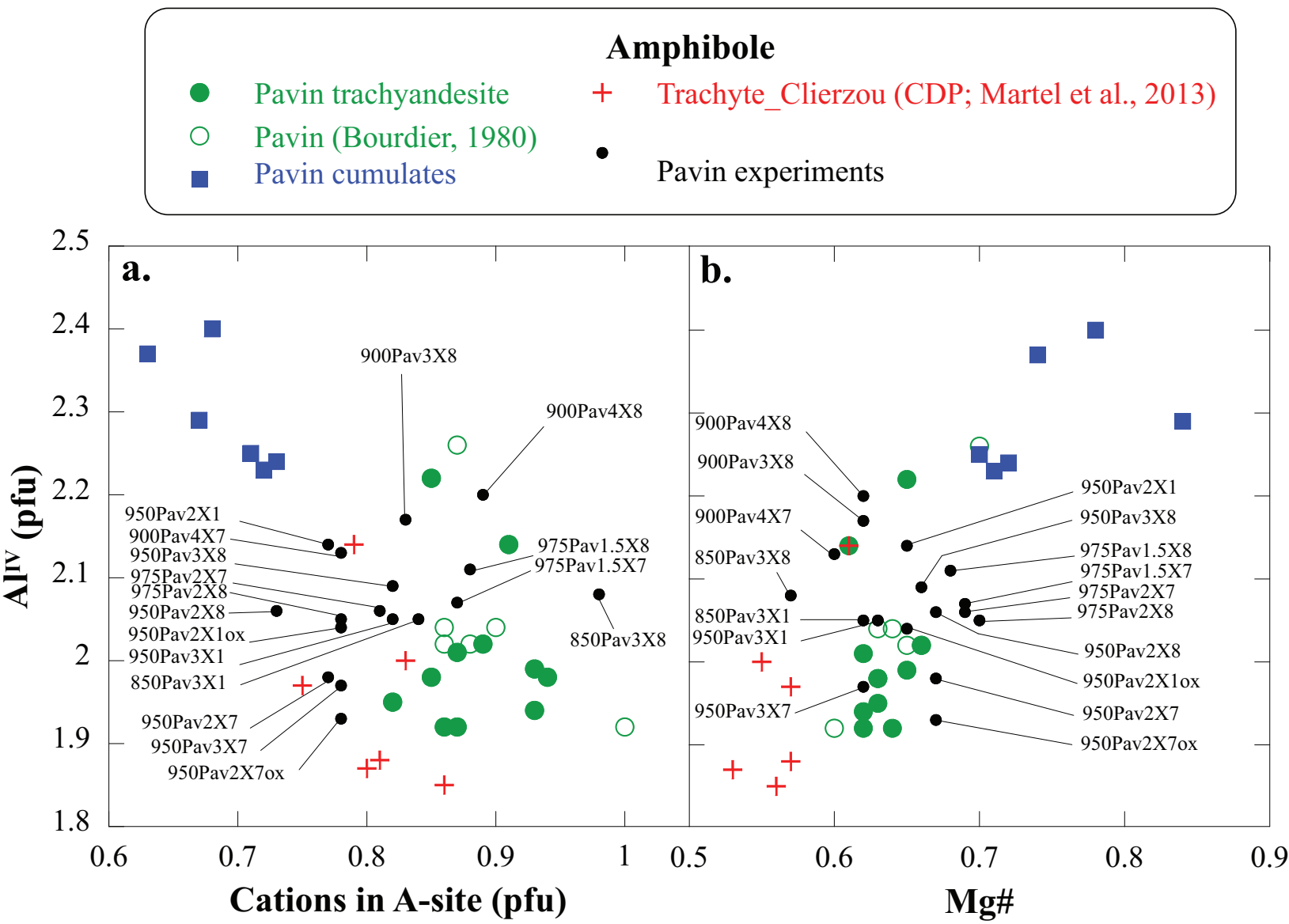
Amphibole
Pavin trachyandesite
Pavin (Bourdier, 1980)
Pavin cumulates
Trachyte_Clierzou (CDP; Martel et al., 2013)
Pavin experiments
a.
b.
AlIV (pfu)
Cations in A-site (pfu)
Mg#
900Pav3X8
900Pav4X8
950Pav2X1
900Pav4X7
950Pav3X8
975Pav2X7
975Pav2X8
950Pav2X8
950Pav2X1ox
950Pav3X1
850Pav3X1
950Pav2X7
950Pav3X7
950Pav2X7ox
975Pav1.5X8
975Pav1.5X7
850Pav3X8

Figure 5

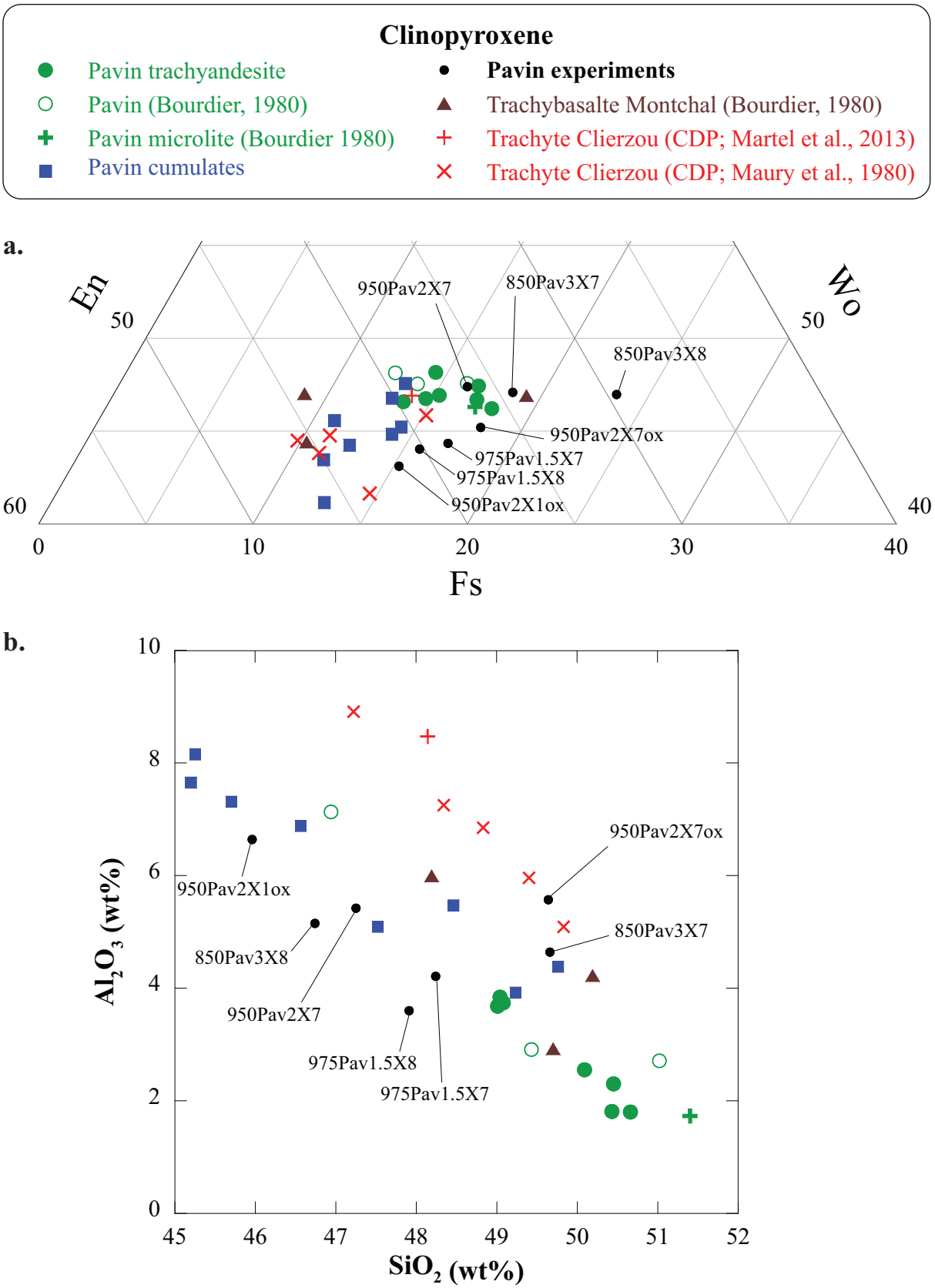
Clinopyroxene
Pavin trachyandesite
Pavin (Bourdier, 1980)
Pavin microlite (Bourdier 1980)
Pavin cumulates
Pavin experiments
Trachybasalte Montchal (Bourdier, 1980)
Trachyte Clierzou (CDP; Martel et al., 2013)
Trachyte Clierzou (CDP; Maury et al., 1980)
a.
En
Wo
Fs
950Pav2X7
850Pav3X7
850Pav3X8
950Pav2X7ox
975Pav1.5X7
975Pav1.5X8
950Pav2X1ox
b.
Al_2O_3 (wt%)
SiO_2 (wt%)
950Pav2X7ox
950Pav2X1ox
850Pav3X7
850Pav3X8
950Pav2X7
975Pav1.5X8
975Pav1.5X7

Figure 6

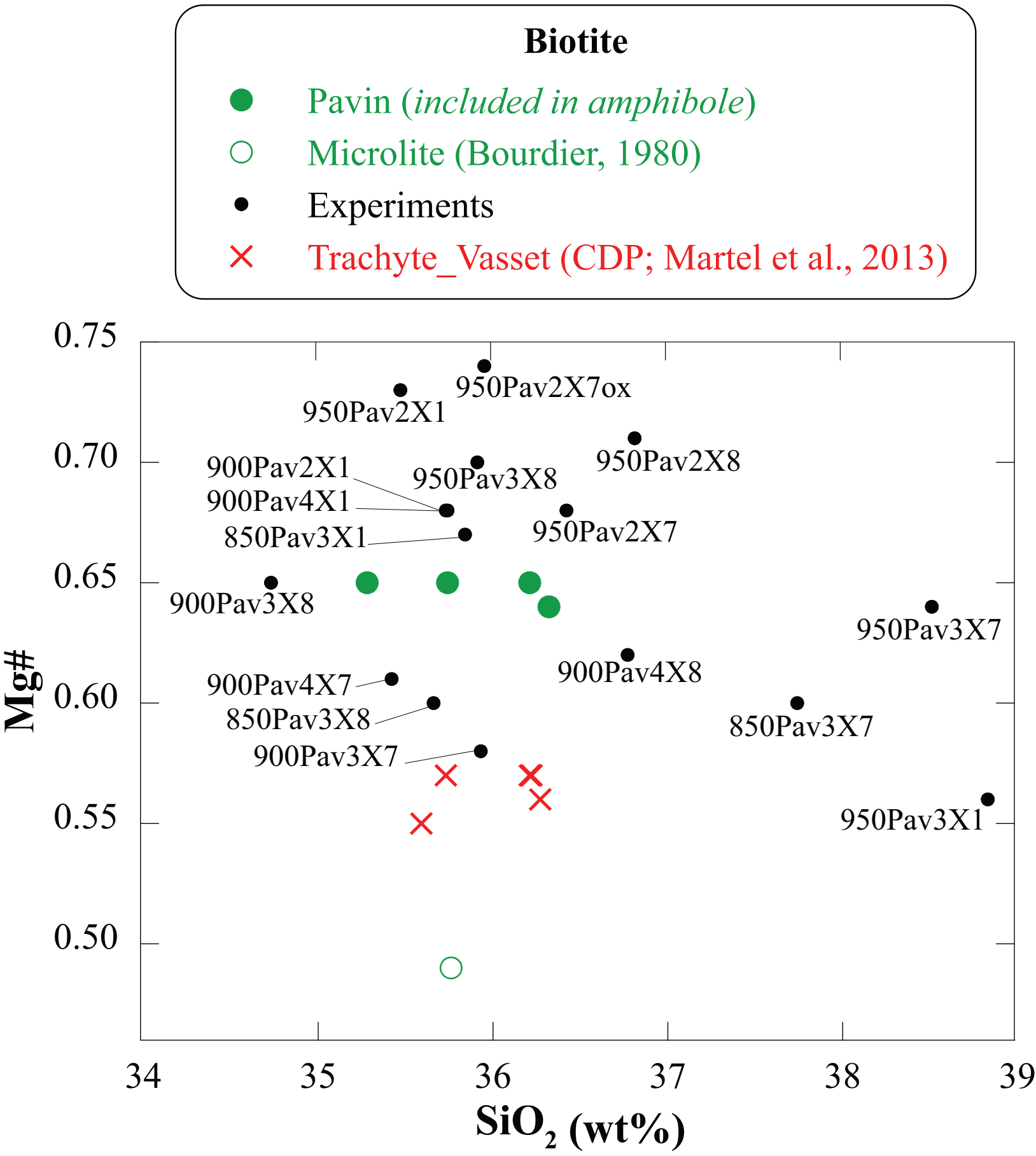
Biotite
Pavin (included in amphibole)
Microlite (Bourdier, 1980)
Experiments
Trachyte_Vasset (CDP; Martel et al., 2013)
950Pav2X7ox
950Pav2X1
950Pav2X8
900Pav2X1
950Pav3X8
900Pav4X1
850Pav3X1
950Pav2X7
900Pav3X8
950Pav3X7
900Pav4X8
900Pav4X7
850Pav3X8
850Pav3X7
900Pav3X7
950Pav3X1
0.75
0.70
0.65
0.60
0.55
0.50
Mg#
34
35
36
37
38
39
SiO2 (wt%)

Figure 7

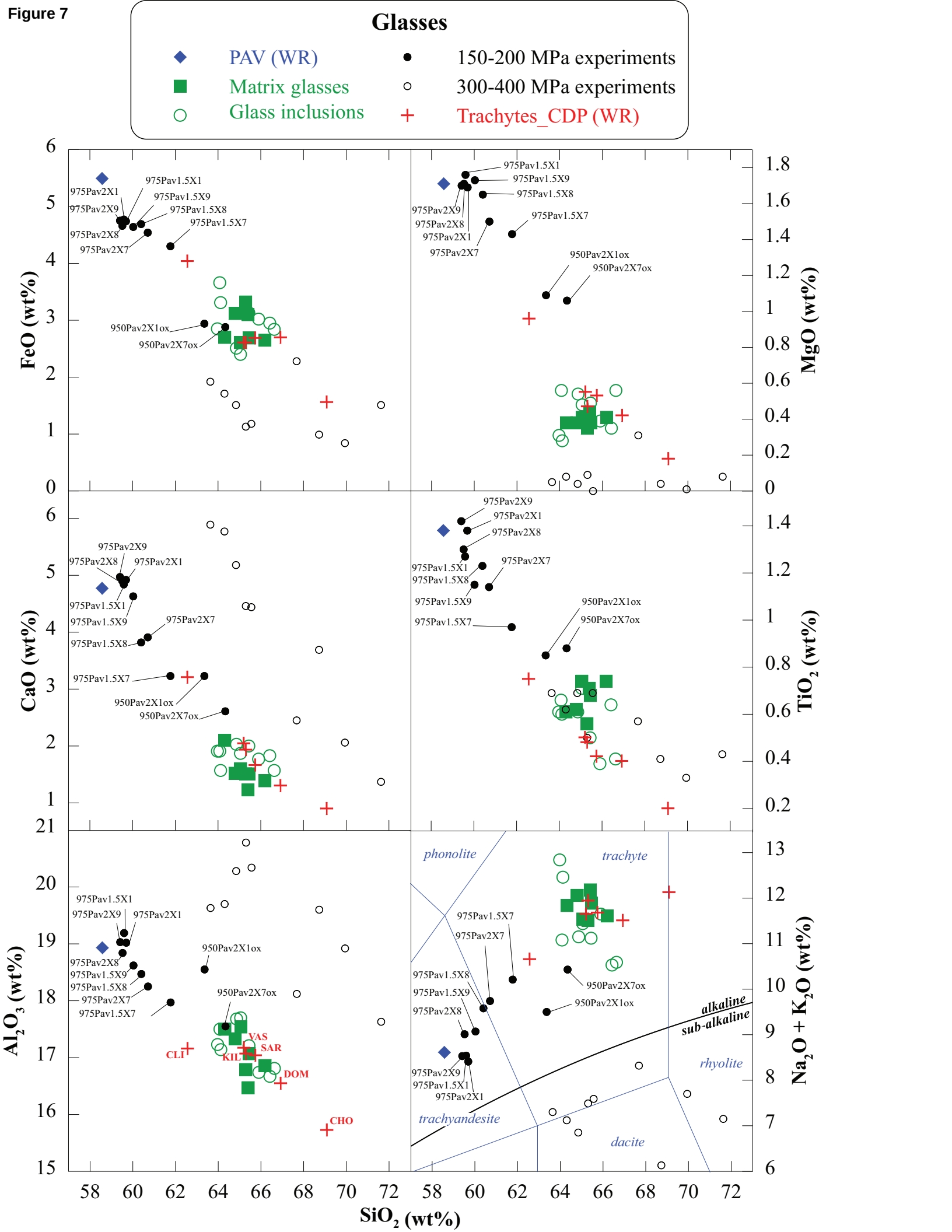
Glasses
PAV (WR)
Matrix glasses
Glass inclusions
150-200 MPa experiments
300-400 MPa experiments
Trachytes_CDP (WR)
FeO (wt%)
MgO (wt%)
CaO (wt%)
TiO2 (wt%)
Al2O3 (wt%)
Na2O + K2O (wt%)
SiO2 (wt%)
975Pav2X1
975Pav1.5X1
975Pav1.5X9
975Pav1.5X8
975Pav1.5X7
975Pav2X9
975Pav2X8
975Pav2X7
950Pav2X1ox
950Pav2X7ox
CLI
VAS
SAR
KIL
DOM
CHO
phonolite
trachyte
rhyolite
trachyandesite
dacite
alkaline
sub-alkaline

Figure 8

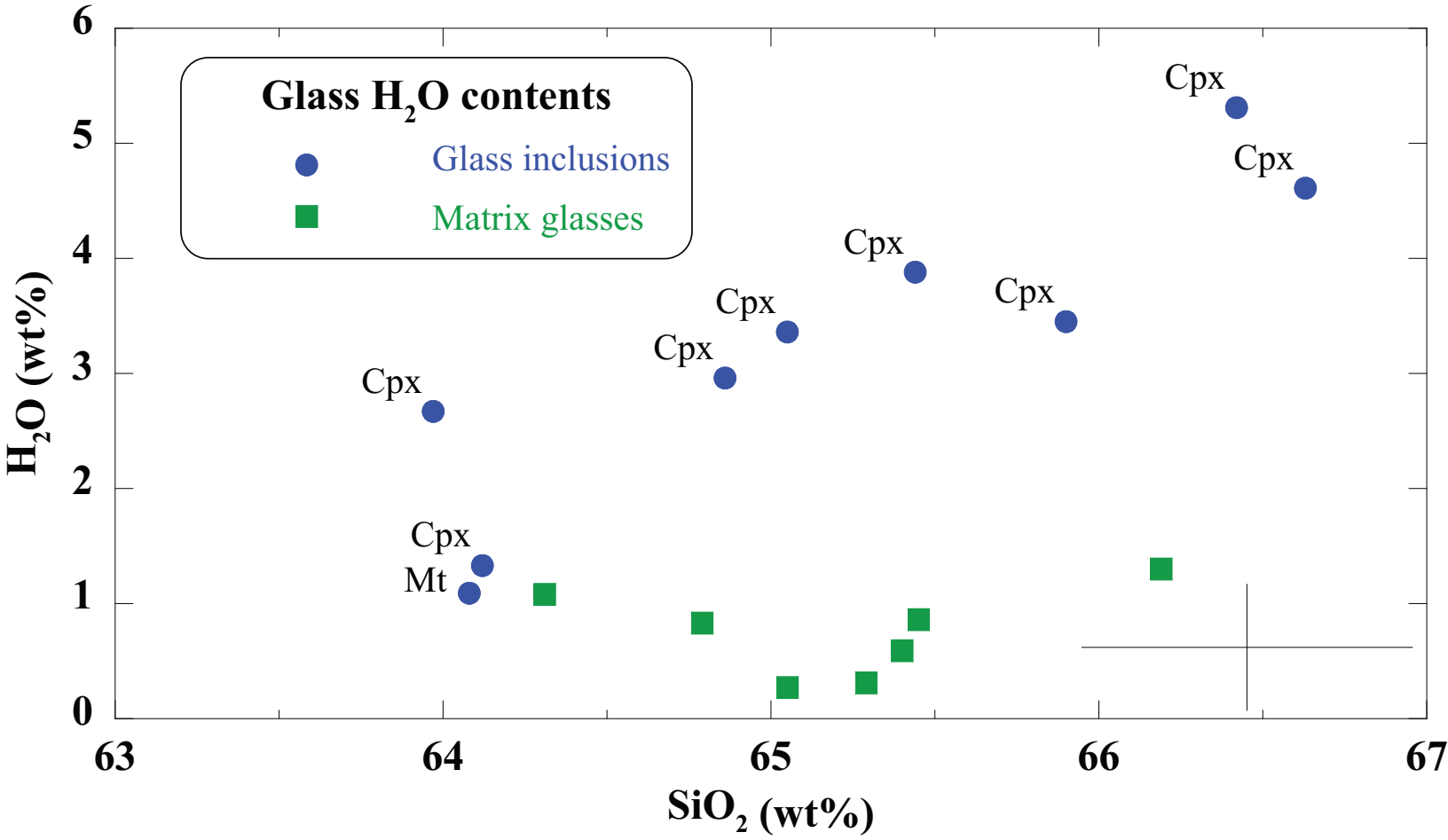
Glass H_2O contents
Glass inclusions
Matrix glasses
Cpx
Cpx
Cpx
Cpx
Cpx
Cpx
Cpx
Mt
6
5
4
3
2
1
0
63
64
65
66
67
H_2O (wt%)
SiO_2 (wt%)

Figure 9

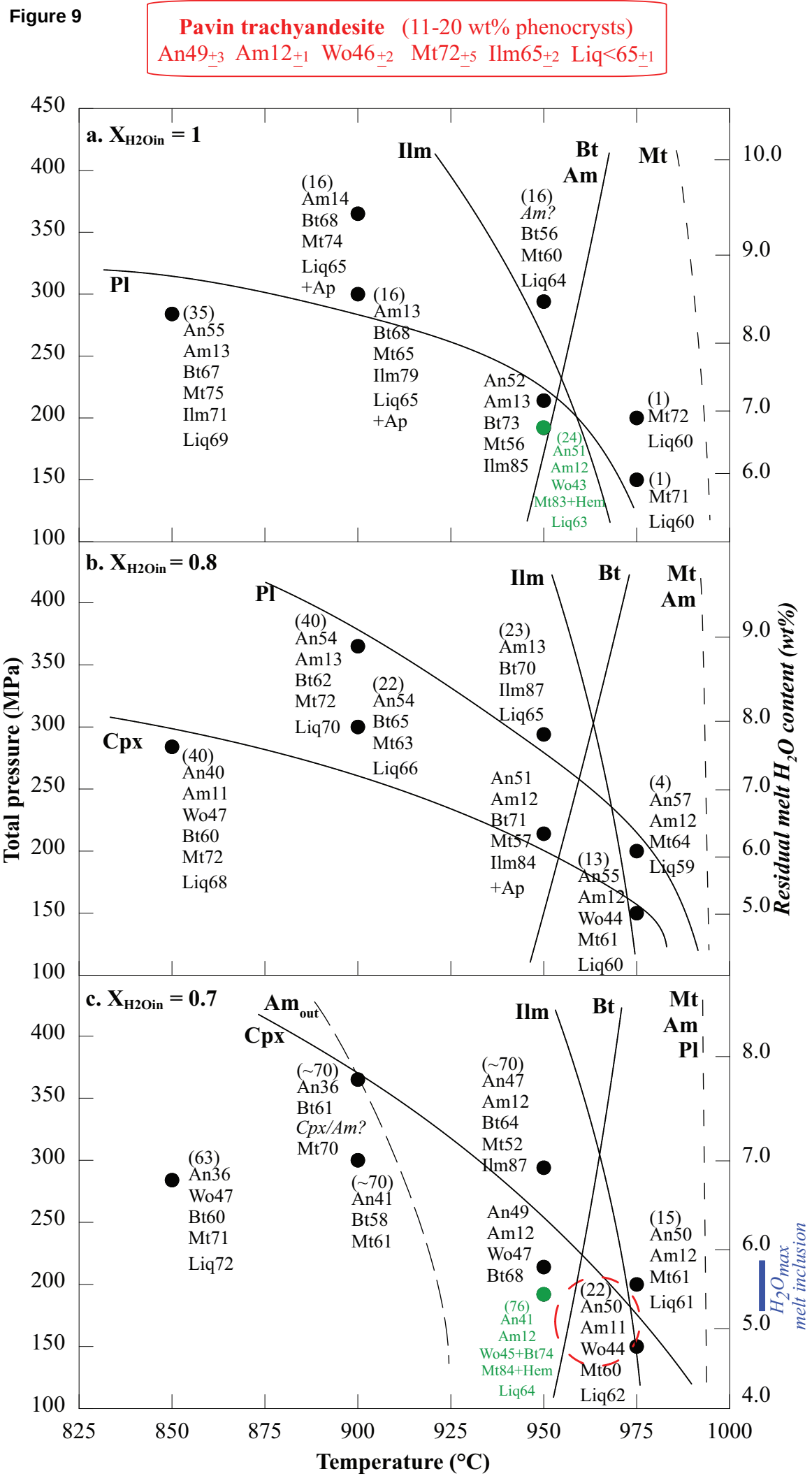
Pavin trachyandesite (11-20 wt% phenocrysts)
An49+3 Am12+1 Wo46+2 Mt72+5 Ilm65+2 Liq<65+1
a. XH2Oin = 1
Ilm
Bt
Am
Mt
Pl
(16) Am14 Bt68 Mt74 Liq65 +Ap
(16) Am13 Bt68 Mt65 Ilm79 Liq65 +Ap
(16) Am? Bt56 Mt60 Liq64
(35) An55 Am13 Bt67 Mt75 Ilm71 Liq69
An52 Am13 Bt73 Mt56 Ilm85
(24) An51 Am12 Wo43 Mt83+Hem Liq63
(1) Mt72 Liq60
(1) Mt71 Liq60
b. XH2Oin = 0.8
Pl
Ilm
Bt
Mt
Am
Cpx
(40) An54 Am13 Bt62 Mt72 Liq70
(22) An54 Bt65 Mt63 Liq66
(23) Am13 Bt70 Ilm87 Liq65
(40) An40 Am11 Wo47 Bt60 Mt72 Liq68
An51 Am12 Bt71 Mt57 Ilm84 +Ap
(4) An57 Am12 Mt64 Liq59
(13) An55 Am12 Wo44 Mt61 Liq60
c. XH2Oin = 0.7
Amout
Cpx
Ilm
Bt
Mt
Am
Pl
(~70) An36 Bt61 Cpx/Am? Mt70
(~70) An41 Bt58 Mt61
(~70) An47 Am12 Bt64 Mt52 Ilm87
(63) An36 Wo47 Bt60 Mt71 Liq72
An49 Am12 Wo47 Bt68
(76) An41 Am12 Wo45+Bt74 Mt84+Hem Liq64
(15) An50 Am12 Mt61 Liq61
(22) An50 Am11 Wo44 Mt60 Liq62
H2Omax melt inclusion
Total pressure (MPa)
Residual melt H2O content (wt%)
Temperature (°C)
100
150
200
250
300
350
400
450
825
850
875
900
925
950
975
1000
4.0
5.0
6.0
7.0
8.0
9.0
10.0

Figure 10

MPa | km

0 - 0

Fragmentation level generating pumice clasts

Residual liq64-66 with 0.3 to 1.2 wt% H_2O

Degassing

50 - 2.0

Upper stage of syn-eruptive crystallization

An30-40

Liq64-66 with ~3 wt% H_2O

Decompression- and/or cooling-induced crystallization as microlites or phenocryst rims; Plagioclase-hosted melt inclusions break-up

Re-equilibration of the melt inclusions upon ascent (3-6 wt% H_2O)

Differentiation of the residual melt along with plagioclase crystallization

100 - 4.0

Magma ascent

150 - 5.5

Reservoir

$An49_{\pm3}$ Am $Wo46_{\pm2}$ $Liq62_{\pm1}$

200 - 7.0

Trachyandesite
950-975 °C ~NNO +1.5
~150-200 MPa (~5.5-7.0 km)
~10-20 wt% phenocrysts
~4.5-5.5 wt% H_2O

Table 1

Major-element composition and CIPW norm of the Pavin group and comparison with samples from the Chaîne des Puys.

	Pavin group					**Chaîne des Puys**		
	Pavin			**Montchal**	**Montcineyre**	**Nugère**	**Clierzou**	
Sample type	fused pumice	dense clast	dense clast	lava sample	lava sample	lava sample	lava sample	fused rock
Reference	this work	1	2	1	1	3	3	4
Major elements (wt %)								
SiO_2	58,57	58,45	57,61	49,23	43,80	57,69	61,60	62,67
TiO_2	1,38	1,30	1,37	2,35	2,80	1,13	0,85	0,75
Al_2O_3	18,93	18,05	17,98	16,40	14,10	18,08	18,32	17,19
Fe_2O_3	*nd*	*nd*	*nd*	*nd*	*nd*	6,90	4,80	*nd*
FeO	5,49	6,11	5,98	9,39	11,16	nd	nd	4,04
MnO	0,12	0,15	0,15	0,17	0,17	0,19	0,23	0,19
MgO	1,71	2,11	1,78	6,88	12,70	1,96	1,09	0,96
CaO	4,77	4,71	4,79	8,97	10,00	4,58	3,17	3,22
Na_2O	4,79	5,01	5,49	3,67	3,20	5,48	5,71	6,59
K_2O	3,82	4,11	4,49	1,97	1,45	3,44	3,91	4,09
P_2O_5	0,40	*nd*	0,37	*nd*	*nd*	0,56	0,32	0,29
Diff. to 100	-1,29	-0,09	0,18	0,97	0,62	0,21	1,98	0,18
Na_2O/Na_2O+K_2O	0,56	0,55	0,55	0,65	0,85	0,61	0,59	0,62
P.I.	0,64	0,70	0,77	0,34	0,33	0,70	0,74	0,89
CIPW norm								
quartz	2,14	-	-	-	-	-	3,63	0,78
orthoclase	22,57	24,29	26,54	11,64	8,62	20,30	23,10	24,15
albite	40,54	42,39	40,96	22,40	3,51	46,34	48,31	55,77
anorthite	18,87	14,62	11,14	22,45	19,95	14,59	12,80	5,24
nepheline	-	-	2,98	4,69	12,86	-	-	-
apatite	0,99	-	0,92	-	-	1,39	0,80	0,73
ilmenite	2,62	2,47	2,60	4,46	5,35	2,15	1,61	1,43
magnetite	1,15	1,28	1,26	1,97	2,36	1,31	0,91	0,85
diopside	1,86	7,31	8,58	17,94	24,1	3,77	0,73	7,48
hypersthene	9,39	4,78	-	-	1,10	6,80	7,75	3,68
olivine	-	2,94	5,18	13,61	23,42	2,87	-	-

Fused sample of the Pavin trachyandesite was analyzed by EMP (corrected for Na loss; Analytical methods given in Appendix A2), all other analyses from the literature, with references as follows: (1) Bourdier, 1980 ; (2) Villemant et al., 2016 ; (3) Maury et al., 1980 ; (4) Martel et al., 2013 (corrected for Na loss). Sum of 10 oxides recalculated on 100% for all analyses, with difference to 100 of the original analyses given (negative when original sum > 100). P.I. is the peralkalinity index given as molar $(Na_2O+K_2O)/Al_2O_3$. *nd* for not determined.

Table 2

Modal proportions of the Pavin pyroclasts.

Reference[a]	This study				(1)		(2)	
Lithology[b]	pumice		pumice		pumice		all	
Proportion[c]	%	*wt%*	%	*wt%*	%	*wt%*	%	*wt%*
Plagioclase	14	*13*	5	*4*	6.5	*6*	6	*6*
Amphibole	4	*3*	3	*2*	2	*1*	7	*6*
Clinopyroxene	1	*2*	1	*1*	1.5	*1*	7	*5*
Fe-Ti oxides	4	*2*	1	*<1*	0.5	*<1*	3	*1*
Crystallinity[c]	23	*20*	10	*7*	10.5	*8*	23	*18*

[a] From (1) Bourdier (1980) and (2) Leyrit et al. (2016).

[b] **pumice** for pumice clasts and **all** denotes analyses on 17 thin sections encompassing pumice to dense clasts (mean mineral content).

[c] **%** gives the void-free modal proportion determined from point counting using an optical microscope and **wt%** is mass proportion recalculated with the respective mineral densities as defined in text.

[d] Plus apatite (<0.5) and very rare biotite.

Table 3

Experimental conditions, phase assemblages and proportions.

Sample #	X_{H2Oin}	H_2O_{melt} (wt%)[a]	Major phases (proportion in wt%)	χ (wt%)[b]	χ_{SiO2} (wt%)[c]
Run 1, 300 MPa, 900°C, NNO+0.8 (sensors), 4 days					
900Pav3X1	1.00	8.5	$Gl_{(84)}$ + $Am_{(3)}$ + $Bt_{(9)}$ + $Mt_{(4)}$ + $Ilm_{(0.2)}$ + Ap	17	36.7
900Pav3X8	~0.9	8.0	$Gl_{(78)}$ + $Am_{(8)}$ + $Bt_{(5)}$ + $Pl_{(5)}$ + $Mt_{(4)}$ + $Ilm_{(0.1)}$	22	41.7
900Pav3X7	0.75	7.4	Gl + Am + Bt + Pl + Mt + Ilm	~70	
Run 2, 294 MPa, 950°C, ~NNO+0.5 (from Fe-Ti oxide thermo-oxymetry), 5 days					
950Pav3X1	1.00	8.5	$Gl_{(83)}$ + $Am_{(<1)}$ + $Bt_{(15)}$ + $Mt_{(2)}$	16	38.8
950Pav3X8	0.84	7.7	$Gl_{(77)}$ + $Am_{(3)}$ + $Bt_{(14)}$ + $Mt_{(5)}$ + $Ilm_{(1)}$	23	36.6
950Pav3X7	0.69	7.0	Gl + Am + Bt + Pl + Mt + Ilm	~70	
Run 3, 284 MPa, 850°C, NNO+0.8 (sensors), 5 days					
850Pav3X1	1.00	8.5	$Gl_{(65)}$ + $Am_{(5)}$ + $Bt_{(9)}$ + $Pl_{(17)}$ + $Mt_{(3)}$ + $Ilm_{(1)}$	35	45.6
850Pav3X8	0.83	7.5	$Gl_{(60)}$ + $Am_{(14)}$ + $Bt_{(3)}$ + $Pl_{(24)}$ + $Cpx_{(7)}$ + $Mt_{(2)}$ + $Ilm_{(0.3)}$	40	48.3
850Pav3X7	0.67	6.7	$Gl_{(60)}$ + $Bt_{(11)}$ + $Pl_{(45)}$ + $Cpx_{(4)}$ + $Mt_{(3)}$ + $Ilm_{(0.6)}$	63	53.8
Run 4, 192 MPa, 950°C, NNO+2.1 (sensors), 8 days					
950Pav2X1ox	1.00	6.9	$Gl_{(76)}$ + $Am_{(5)}$ + $Pl_{(15)}$ + $Cpx_{(0.5)}$ + $Mt_{(2)}$ + $Hem_{(2)}$	24	50.2
950Pav2X7ox	~0.75	5.7	$Gl_{(24)}$ + $Am_{(15)}$ + $Bt_{(10)}$ + $Pl_{(36)}$ + $Cpx_{(11)}$ + $Mt_{(3)}$ + $Hem_{(1)}$	76	49.9
Run 5, 365 MPa, 900°C, ~NNO+1.5 (from Fe-Ti oxide thermo-oxymetry), 4.5 days					
900Pav4X1	1.00	9.5	$Gl_{(84)}$ + $Am_{(4)}$ + $Bt_{(7)}$ + $Mt_{(4)}$ + $Ilm_{(<1)}$ + $Ap_{(1)}$	16	36.5
900Pav4X8	0.80	8.3	$Gl_{(60)}$ + $Am_{(11)}$ + $Bt_{(6)}$ + $Pl_{(20)}$ + $Mt_{(3)}$ + $Ilm_{(1)}$	40	45.9
900Pav4X7	~0.70	7.8	Gl + Am/Cpx + Bt + Pl + Mt + Ilm	~70	
Run 6, 214 MPa, 950°C, NNO+0.7 (sensors), ~2 days *(failed)*					
950Pav2X1	1.00	6.9	Gl + Am + Bt + Pl + Mt + Ilm	-	
950Pav2X8	0.76	6.3	Gl + Am + Bt + Pl + Mt + Ilm + Ap	-	
950Pav2X7	0.67	5.8	Gl + Am + Bt + Pl + Cpx + Mt + Ilm	-	
Run 7, 192 MPa, 975°C, ~NNO+1 (no sensors), 7.5 days					
975Pav2X1	1.00	6.9	$Gl_{(99)}$ + $Mt_{(1)}$	1	
975Pav2X9	0.90	6.6	$Gl_{(99)}$ + $Mt_{(1)}$	1	
975Pav2X8	0.77	6.3	$Gl_{(96)}$ + $Am_{(1)}$ + $Pl_{(2)}$ + $Mt_{(1)}$	4	47.9
975Pav2X7	0.68	5.8	$Gl_{(85)}$ + $Am_{(2)}$ + $Pl_{(11)}$ + $Mt_{(2)}$	15	51.5
Run 8, 148 MPa, 975°C, ~NNO+1 (no sensors), 4 days					
975Pav1.5X1	1.00	5.8	$Gl_{(99)}$ + $Mt_{(1)}$	1	
975Pav1.5X9	0.89	5.4	$Gl_{(93)}$ + $Pl_{(5)}$ + $Mt_{(2)}$	7	51.7
975Pav1.5X8	0.77	5.0	$Gl_{(87)}$ + $Am_{(1)}$ + $Pl_{(9)}$ + $Cpx_{(2)}$ + $Mt_{(1)}$	13	50.0
975Pav1.5X7	0.69	4.5	$Gl_{(78)}$ + $Am_{(1)}$ + $Pl_{(17)}$ + $Cpx_{(2)}$ + $Mt_{(2)}$	22	52.1

[a] Melt H_2O content calculated after *equation* (1).

[b] Crystallinity.

[c] SiO_2 content in wt% of the cumulate (Am, Bt, Pl, Cpx) calculated as the sum of the mass fractions of each mineral (from the '**Major phase**' column, divided by the total fraction) by each mineral SiO_2 contents (as given in Appendix B1-4).

Appendix A (Methods).

A1. Experimental methods

Starting material and experimental charges. Crystallization experiments were performed starting from trachyandesitic pumices sampled in the Clidères section of Leyrit et al. (2016), 1 km south of the Pavin crater rim (Fig. 1). A tenth of macroscopically homogeneous pumiceous clasts was ground into fine powder (~20 µm) and fused in a Pt-crucible at 1400 °C and 1 atm for 2 h, air-quenched and powdered in a mortar. The cycle of fusion and grinding was repeated twice to ensure chemical homogeneity of the starting glass powder (PAV). The EMP analyses show that the PAV composition is close to the respective whole-rock ones (Table 1). Charges consisted of ~30 mg of PAV glass powder, added to deionized H_2O, and silver oxalate as source of CO_2, which were introduced in Au containers (2.5 mm inner diameter, 0.2 mm wall thickness, and 20 mm length) sealed by arc-welding and checked for leakage by immersion in an oil bath at 120 °C. All experiments were vapour-saturated, either with pure H_2O (X_{H2Oin} = $X_{H2O}/(X_{H2O}+X_{CO2})$ = 1, in moles) or with a H_2O-CO_2 fluid mixture (X_{H2Oin} from ~0.7 to 0.9). The fluid/silicate ratio was kept constant around 10 wt% to avoid significant changes in the silicate composition.

Equipments. All experiments were performed in vertically-working internally-heated pressure vessels pressurized with Ar-H_2 gas mixtures. Up to four capsules (containing PAV with three different X_{H2Oin} and one redox sensor; see below) were placed at the hotspot of a Mo- or K-windings furnace where the thermal gradient over ~3 cm is less than 5 °C. The furnace temperature was regulated by a Eurotherm controller and temperature (*T*) was read continuously by S-type thermocouples with typical uncertainty of ±5 °C. Total pressure (*P*) was recorded continuously by a transducer calibrated against a Heise Bourdon gauge (±0.4 MPa). Run durations varied between 3 and 5 days, depending on *T*, in agreement with run durations in Martel et al. (2013). The experiments were stopped either by isobaric quench (by switching off the furnace while maintaining *P* constant) or by rapid quench (using a device allowing capsule drop in the cold part of the furnace with a cooling rate of ~100 °C/s; modified after Roux and Lefevre, 1992). After experiments, each capsule was weighed to check for leakage and opened. Clasts of the samples were embedded in epoxy resins for analysis.

Control of redox conditions. The redox state of the experimental charges was controlled by the H_2 fugacity of the Ar-H_2 gas pressure medium. Half of the runs contained Ni-Pd-O solid sensors that were used to measure the experimental H_2 fugacity following the method of Pownceby and O'Neill (1994). The oxygen fugacity (f_{O2}) was finally calculated from the H_2O dissociation reaction that requires the H_2O fugacity determined from the H_2O content of the experimental glasses following the model of Burnham (1979). The resulting uncertainty on log f_{O2} is $\pm$0.3 log unit (Martel et al., 1999).

A2. Analytical methods

Textural assessment and major-element analysis. The textural characteristics of the natural and experimental samples were examined using a scanning electron microscope (SEM; MIRA3 TESCAN at ISTO). SEM imaging allowed identification of minerals or glass areas for chemical analysis using an electron microprobe (EMP; SX Five at ISTO). The analytical conditions for the natural and experimental crystals were set to an acceleration voltage of 15 kV, a beam current of 10 nA, and a focused beam (spot size < 2 µm). Both peak and background counting times were set at 10 s for all elements. The redox sensors were analysed for S, Fe, Co, Ni, Pd, Pt and Au (using metallic elements and pyrite standards) with a beam current of 20 nA (15 kV and 10 s counting time). Glasses were analysed with a beam current of 6 nA, 15 k, 10 s counting time, and a defocused 10 µm² beam size to minimize alkali migration under the electron beam. However, alkali- and H_2O-rich compositions such as those of the Pavin trachyandesite commonly need to be corrected for Na migration (Pichavant, 1987). Therefore, in agreement with the analyses of the trachytic glasses from the Chaîne des Puys (Martel et al., 2013), we applied a similar correction factor of 1.2 for Na_2O on the analyses of the Pavin glasses on the ground that they are chemically close and were run at comparable *P*-*T*-H_2O conditions. The analytical errors on major elements were calculated at ~1% (relative) for SiO_2, Al_2O_3 and CaO, 3% for FeO, MgO and TiO_2, and 5% for MnO, Na_2O and K_2O.

Melt H_2O contents. The H_2O contents of the glass inclusions and residual glasses of the pumice samples were measured by EMP using a modified by-difference method (Devine et al., 1995), which requires calibration of the differences to 100 wt% of the glass EMP analyses against chemically-close glass standards whose H_2O contents are known and bracket the

range of those anticipated for the samples. As glass standards, we used two trachytic glasses (800CHO2 and 800CHO3) containing 6.9 and 8.5 wt% H_2O (determined by Karl-Fisher titration) as defined in Martel et al. (2013). The resulting uncertainty on H_2O content measurements is ±0.5 wt% absolute.

H_2O contents could not be measured in all experimental glasses because of glass areas often too small in sizes for EMP analyses. The H_2O-pressure (*P*) empirical equation of Di Matteo et al. (2004) calculates H_2O solubility for trachytic liquids at 850-895 °C up to *P* of 200 MPa. To extrapolate this formulation to higher *P*, we used the near-liquidus trachytic glasses obtained by Martel et al. (2013) who reported $6.9_{\pm 0.5}$ wt% H_2O in the 800 °C and 200 MPa glass (in good agreement with the $7.2_{\pm 0.8}$ wt% H_2O calculated after Di Matteo et al., 2004) and $8.5_{\pm 0.5}$ wt% at 300 MPa and 800 °C. Following a logarithmic law of the form below, we extrapolated H_2O solubility at 400 MPa to be close to 9.5 wt% H_2O:

$$H_2O\ (wt\%) = 3.76*Ln[P\ (MPa)]-13.0 \qquad equation\ (1)$$

H_2O contents in H_2O-undersaturated charges were approximated by $P \sim P_{total}*X_{H2Oin}$.

Phase proportions. In the natural samples, modal proportions of phenocrysts and void-free groundmass were obtained by point counting on two thin sections (~1200 points) using an optical microscope. The error related to this method is estimated to ±10% relative. Because the experimental minerals are commonly too small (<20 µm) to be clearly identified using an optical microscope, the phase proportions were determined by mass balance using the formulation of Stormer and Nicholls (1978) and the EMP chemical compositions of the crystals, residual glasses, and bulk rock. To compare both methods, the modal proportions of the natural samples were converted into wt% using the following mineral densities: 2.7 for feldspars (andesine), 5.2 for magnetite and ilmenite, 3.0 for biotite, 3.3 for clinopyroxene (augite), 3.2 for amphibole (pargasite), 3.0 for biotite, and 2.4 for the glass.

References

Burnham, C. W., 1979. The importance of volatiles constituents. In: Yoder, H.S. (Ed.), The Evolution of the Igneous Rocks: Fifth Anniversary Perspectives. Princeton, NJ: Princeton University Press, pp. 439–482.

Devine, J. D., Gardner, J. E., Brack, H. P., Layne, G. D., Rutherford, M. J., 1995. Comparison of microanalytical methods for estimating H_2O contents of silicic volcanic glasses. Am. Mineral. 80, 319-328.

Martel, C., Pichavant, M., Holtz, F., Scaillet, B., Bourdier, J.-L., Traineau, H., 1999. Effect of fO_2 and H_2O on andesite phase relations between 2 and 4 kbars. J. Geophys. Res. 104, 29453-29470.

Pichavant, M., 1987. The effects of boron and water on liquidus phase relations in the haplogranite at 1 kbar. Am. Mineral. 72, 1056-1070.

Pownceby, M.I., O'Neil, H., 1994. Thermodynamic data from redox reactions at high temperature. III. Activity-composition relations in Ni-Pd alloys from EMF measurements at 850-1250 K, and calibration of the NiO-Ni-Pd assemblage as a redox sensor. Contrib. Mineral. Petrol. 116, 327-339.

Roux, J., Lefevre, A., 1992. A fast quench device for IHPV. Eur. J. Mineral. 4, 279-281.

Stormer, J.C., Nicholls J., 1978. XLFRAC: a program for the interactive testing of magmatic differentiation models. Comput. Geosci. 4, 143-159.

Appendix B (Natural and experimental compositions).

B1. Plagioclase

Type[a]	Sample#	n	SiO_2		TiO2		Al_2O_3		FeO		MnO		MgO		CaO		Na_2O		K_2O		P_2O_5	F	Total	Or	Ab	An
Natural (selected)																										
core	PAV-P1-01-3		54,44		0,00		27,03		0,34		0,05		0,01		10,52		5,53		0,45		0,00	0,19	98,56	2,53	47,51	49,96
core	PAV-P1-04-4		55,32		0,08		26,03		0,35		0,00		0,06		9,34		6,12		0,54		0,00	0,21	98,05	3,07	52,60	44,33
core	PAV-P1-05-2		58,40		0,02		23,93		0,35		0,00		0,03		6,78		7,36		0,97		0,00	0,09	97,93	5,42	62,68	31,90
core	PAV-P1-15-1		57,54		0,00		25,00		0,35		0,07		0,03		7,99		6,70		0,81		0,00	0,00	98,49	4,56	57,50	37,93
core	PAV-P1-15-3		55,40		0,01		26,45		0,28		0,00		0,01		9,30		6,08		0,54		0,00	0,48	98,55	3,04	52,54	44,41
core	P20-P1-25		55,29		0,04		26,01		0,45		0,11		0,05		9,18		6,08		0,56		0,00	0,35	98,12	3,19	52,78	44,03
core	P20-P1-26		57,65		0,10		25,18		0,43		0,00		0,00		8,16		6,52		0,81		0,15	0,00	99,00	4,63	56,37	38,99
rim	PavP115plgbo		58,32		0,00		24,95		0,35		0,00		0,03		8,02		6,54		0,73		0,00	0,00	98,94	4,20	57,09	38,71
core*	9		52,75		0,10		28,88		0,40		0,00		0,06		11,74		4,54		0,37		0,00	*nd*	98,84	2,16	40,28	57,56
core*	10		57,78		0,00		25,79		0,41		0,08		0,00		7,94		6,77		0,83		0,06	*nd*	99,66	4,67	57,84	37,49
core*	11		55,24		0,05		26,83		0,33		0,00		0,02		8,91		6,04		0,61		0,02	*nd*	98,05	3,53	53,15	43,32
core*	12		58,25		0,00		25,54		0,38		0,02		0,03		7,22		6,93		0,89		0,00	*nd*	99,26	5,09	60,23	34,68
core**	Cum1_11		51,92		0,14		28,17		0,71		0,07		0,06		11,47		4,35		0,37		0,00	0,00	97,26	2,16	40,28	57,56
core**	Cum1_13		53,09		0,17		27,85		0,78		0,01		0,08		11,21		4,55		0,34		0,07	0,22	98,37	4,67	57,84	37,49
core**	Cum3_4		56,80		0,11		24,74		0,78		0,00		0,04		7,87		6,44		1,00		0,03	0,00	97,81	3,53	53,15	43,32
Experimental (average)																										
1	900Pav3X8	2	53,58	*0,67*	0,15	*0,07*	27,17	*0,12*	0,65	*0,02*	0,03	*0,00*	0,03	*0,01*	11,04	*0,18*	4,73	*0,67*	0,57	*0,18*	0,10	0,11	98,16	3,32	42,24	54,44
	900Pav3X7	1	59,25		0,20		25,93		0,41		0,07		0,07		8,23		5,88		1,06		0,00	0,00	101,1	6,25	52,84	40,91
2	950Pav3X7	3	56,58	*1,08*	0,09	*0,05*	26,23	*0,75*	0,51	*0,04*	0,01	*0,01*	0,04	*0,02*	9,69	*0,80*	5,39	*0,40*	0,81	*0,22*	0,17	0,12	99,62	4,73	47,78	47,49
3	850Pav3X1	4	52,81	*0,64*	0,02	*0,01*	27,56	*0,61*	0,47	*0,08*	0,01	*0,01*	0,04	*0,03*	11,04	*0,36*	4,69	*0,29*	0,38	*0,04*	0,00	0,00	97,01	2,26	42,49	55,25
	850Pav3X8	1	57,23		0,10		25,27		0,64		0,06		0,03		8,21		6,18		0,77		0,05	0,00	98,54	4,54	55,08	40,39
	850Pav3X7	2	58,11	*0,54*	0,09	*0,12*	23,84	*0,34*	0,77	*0,01*	0	*0,00*	0,09	*0,03*	7,12	*0,41*	6,30	*0,14*	1,02	*0,07*	0,06	0,00	97,40	6,16	57,75	36,09
4	950Pav2X1ox	4	53,78	*0,71*	0,02	*0,02*	26,99	*0,58*	0,87	*0,03*	0,02	*0,03*	0,05	*0,01*	10,55	*0,42*	5,20	*0,11*	0,48	*0,04*	0,08	0,24	98,28	2,79	45,85	51,36
	950Pav2X7ox	3	57,02	*0,74*	0,07	*0,07*	24,30	*0,71*	0,81	*0,12*	0,06	*0,02*	0,09	*0,04*	7,85	*0,21*	6,06	*0,52*	1,06	*0,14*	0,22	0,20	97,55	6,34	54,53	40,62
5	900Pav4X8	4	53,17	*0,50*	0,00	*0,00*	28,17	*0,37*	0,47	*0,11*	0,04	*0,06*	0,05	*0,01*	10,94	*0,03*	4,75	*0,12*	0,45	*0,03*	0,00	0,00	98,04	2,66	42,82	54,52
	900Pav4X7	2	58,78	*1,95*	0,06	*0,06*	24,46	*1,44*	0,57	*0,10*	0,00	*0,00*	0,01	*0,01*	7,13	*1,37*	5,90	*0,14*	1,61	*0,66*	0,00	0,00	98,52	9,77	54,12	36,11
6	950Pav2X1	1	54,21		0,36		24,91		1,59		0,12		0,51		9,32		3,86		1,26		0,17	0,00	96,30	8,45	39,19	52,36
	950Pav2X8	1	54,51		0,29		26,21		0,88		0,09		0,27		10,06		4,76		0,73		0,00	0,00	97,79	4,46	44,09	51,44
	950Pav2X7	1	54,68		0,37		26,69		1,13		0,14		0,31		9,56		5,06		0,65		0,04	0,00	98,60	3,96	46,98	49,06
7	975Pav2X8	5	52,17	*0,58*	0,14	*0,05*	27,53	*0,68*	0,82	*0,07*	0,05	*0,06*	0,16	*0,05*	11,67	*0,52*	4,47	*0,28*	0,54	*0,07*	*nd*	*nd*	97,54	3,15	39,62	57,22
	975Pav2X7	3	53,67	*0,48*	0,13	*0,13*	26,94	*0,16*	0,65	*0,10*	0,03	*0,05*	0,08	*0,02*	10,46	*0,08*	5,34	*0,02*	0,55	*0,10*	*nd*	*nd*	97,85	3,16	46,51	50,34
8	975Pav1.5X9	7	51,74	*0,36*	0,09	*0,10*	27,38	*0,39*	0,75	*0,16*	0,03	*0,05*	0,09	*0,03*	11,45	*0,54*	4,76	*0,30*	0,46	*0,07*	*nd*	*nd*	96,75	2,65	41,81	55,54

	975Pav1.5X8	3	51,74	*0,33*	0,14	*0,01*	27,48	*0,39*	0,74	*0,13*	0,09	*0,05*	0,08	*0,04*	11,46	*0,34*	4,87	*0,07*	0,53	*0,10*	*nd*	*nd*	97,12	3,02	42,16	54,82
	975Pav1.5X7	3	53,27	*0,92*	0,05	*0,05*	26,71	*0,87*	0,72	*0,07*	0,01	*0,01*	0,09	*0,01*	10,45	*1,11*	5,31	*0,47*	0,68	*0,19*	*nd*	*nd*	97,30	3,87	46,08	50,04

[a]For the natural plagioclases, core or rim analyses; * for data from Bourdier (1980) and ** for cumulate analyses; For the experimental plagioclases, run number as in Table 3. All oxides in wt%, with number of analyses (**n**) and statistical errors (italic numbers) for the experimental compositions. **Or, Ab, An** give the orthoclase, albite, and anorthite molar %, respectively; *nd* for not determined.

B2. Amphibole

Type[a]	Sample#	n	SiO_2	TiO_2	Al_2O_3	FeO	MnO	MgO	CaO	Na_2O	K_2O	P_2O_5	F	Total	A_Cat	Al^{IV}	Mg#
Natural (selected)																	
core	PAV-P1-01-1		38,77	5,28	12,40	13,63	0,02	11,54	11,86	2,73	1,00	0,00	0,33	97,56	0,91	2,14	0,61
rim	PAV-P1-01-2		40,71	4,32	11,33	14,09	0,36	11,82	11,68	2,56	1,35	0,00	0,00	98,22	0,87	1,92	0,62
core	PAV-P1-04		39,38	4,85	11,46	12,32	0,25	12,42	11,59	2,62	1,18	0,00	0,88	96,95	0,89	2,02	0,66
rim	PAV-P1-04-2		39,22	4,22	11,14	14,83	0,39	11,89	11,44	2,64	1,57	0,00	0,00	97,34	0,93	1,99	0,65
core	PAV-P1-04-5		40,19	4,16	11,46	15,33	0,49	11,53	11,54	2,66	1,37	0,00	0,52	99,25	0,87	2,01	0,62
core	PAV-P1-05-1		40,14	4,56	11,61	13,79	0,45	11,73	11,41	2,55	1,44	0,00	0,02	97,7	0,85	1,98	0,63
core	PAV-P1-14-1		40,02	4,46	11,58	13,10	0,30	11,76	11,75	2,60	1,33	0,00	0,18	97,08	0,93	1,94	0,62
core	P20-P1-32		38,46	5,13	12,69	13,98	0,15	11,64	11,25	2,72	1,27	0,04	0,59	97,92	0,85	2,22	0,65
core	P20-P1-38		40,20	4,07	11,30	14,25	0,22	12,15	11,73	2,68	1,47	0,00	0,77	98,84	0,94	1,98	0,63
rim	PavP115bo		40,35	4,79	11,82	13,03	0,23	11,90	11,46	2,48	1,33	0,02	0,00	97,41	0,82	1,95	0,63
core	PavP115co		40,75	4,66	11,37	13,14	0,29	12,23	11,56	2,64	1,29	0,12	0,36	98,41	0,86	1,92	0,64
core*	6		40,01	4,92	13,07	12,10	0,00	11,96	11,75	2,59	1,27	*nd*	*nd*	97,67	0,86	2,04	0,64
core*	7		40,45	4,14	11,59	13,76	0,48	11,61	11,45	2,97	1,60	*nd*	*nd*	98,05	1,00	1,92	0,60
core*	8		40,32	4,56	12,57	12,74	0,27	12,22	11,58	2,68	1,40	*nd*	*nd*	98,34	0,88	2,02	0,65
core*	9		39,44	4,57	12,65	12,89	0,08	11,67	11,33	2,87	1,17	*nd*	*nd*	96,67	0,90	2,04	0,63
core*	10		38,86	5,90	13,96	10,05	0,05	13,15	12,19	2,50	1,20	*nd*	*nd*	97,86	0,87	2,26	0,70
core*	11		39,89	4,63	12,26	12,43	0,07	12,40	11,52	2,67	1,24	*nd*	*nd*	97,11	0,86	2,02	0,66
core**	Cum1_1		38,57	6,05	13,71	10,76	0,12	12,57	11,44	2,32	1,05	0,01	0,25	96,85	0,71	2,25	0,70
core**	Cum1_3		37,27	5,32	14,51	14,11	0,21	10,56	11,50	2,37	0,95	0,01	0,00	96,81	0,63	2,37	0,74
core**	Cum1_4		38,36	5,68	13,29	10,67	0,00	12,96	11,45	2,28	1,11	0,05	0,33	96,16	0,73	2,24	0,72
core**	Cum1_5		38,85	5,55	13,71	11,07	0,14	12,68	11,57	2,26	1,15	0,00	0,00	96,98	0,72	2,23	0,71
core**	Cum3_1		37,06	5,35	14,09	13,25	0,07	11,58	11,45	2,49	1,03	0,06	0,35	96,79	0,68	2,40	0,78
core**	Cum3_2		37,52	4,93	13,35	12,86	0,21	11,72	11,52	2,55	1,07	0,18	0,17	96,07	0,67	2,29	0,84
Experimental (average)																	
1	900Pav3X1	3	39,51	*0,93*	3,54	*0,21*	13,05	*0,26*	12,81	*0,60*	0,22	*0,02*	12,01	*0,35*	11,77	*0,14*	2,40	*0,06*	1,13	*0,05*	0,03	0,14	96,60	0,82	2,05	0,63
	900Pav3X8	3	38,73	*0,16*	3,72	*0,49*	13,31	*0,66*	13,40	*0,72*	0,22	*0,22*	11,90	*0,19*	11,80	*0,20*	2,40	*0,03*	1,18	*0,03*	0,10	0,23	97,00	0,83	2,17	0,62
2	950Pav3X8	3	39,62	*0,41*	4,33	*0,34*	12,98	*0,21*	11,73	*0,61*	0,18	*0,06*	12,78	*0,21*	11,73	*0,14*	2,47	*0,11*	1,22	*0,06*	0,10	0,01	97,13	0,82	2,09	0,66

	950Pav3X7	3	40,33	*0,28*	4,31	*0,13*	12,03	*0,36*	13,32	*0,14*	0,27	*0,03*	11,95	*0,31*	11,46	*0,10*	2,51	*0,06*	1,12	*0,06*	0,04	0,21	97,55	0,78	1,97	0,62
3	850Pav3X1	3	38,88	*0,68*	3,26	*0,10*	12,57	*0,51*	13,28	*0,47*	0,20	*0,06*	11,80	*0,20*	11,50	*0,36*	2,39	*0,01*	1,25	*0,03*	0,28	0,19	95,61	0,84	2,05	0,62
	850Pav3X8	1	36,38		3,52		10,94		14,48		0,33		10,67		13,00		2,31		1,25		1,39	0,11	94,37	0,98	2,08	0,57
4	950Pav2X1ox	6	40,36	*0,85*	3,68	*0,22*	11,97	*0,22*	10,91	*0,53*	0,35	*0,17*	14,42	*0,41*	11,66	*0,16*	2,54	*0,15*	1,12	*0,06*	0,13	0,19	97,34	0,78	2,04	0,65
	950Pav2X7ox	4	41,07	*0,67*	3,99	*0,13*	11,44	*0,29*	10,38	*0,42*	0,33	*0,22*	14,34	*0,17*	11,38	*0,04*	2,62	*0,09*	1,21	*0,11*	0,07	0,24	96,76	0,78	1,93	0,67
5	900Pav4X1	3	37,79	*0,39*	3,05	*0,08*	13,82	*0,17*	12,74	*0,38*	0,25	*0,10*	11,72	*0,29*	12,28	*0,41*	2,22	*0,02*	1,27	*0,11*	0,50	0,00	95,70	0,89	2,20	0,62
	900Pav4X8	4	38,90	*0,48*	3,70	*0,27*	13,09	*0,11*	14,09	*0,22*	0,33	*0,09*	11,40	*0,06*	11,41	*0,14*	2,35	*0,05*	1,31	*0,11*	0,10	0,00	96,67	0,78	2,13	0,60
6	950Pav2X1	3	39,06	*0,55*	4,49	*0,27*	12,85	*0,04*	11,61	*0,15*	0,30	*0,03*	12,81	*0,17*	11,63	*0,31*	2,32	*0,09*	1,19	*0,11*	0,12	0,00	96,40	0,77	2,14	0,65
	950Pav2X8	3	39,61	*0,43*	4,75	*0,27*	12,12	*0,44*	11,37	*0,70*	0,19	*0,15*	13,22	*0,39*	11,36	*0,13*	2,36	*0,06*	1,14	*0,09*	1,10	0,10	96,20	0,73	2,06	0,67
	950Pav2X7	4	40,11	*0,62*	4,72	*0,28*	11,75	*0,28*	12,08	*0,32*	0,23	*0,05*	12,65	*0,41*	11,30	*0,10*	2,51	*0,11*	1,15	*0,12*	0,10	0,00	96,60	0,77	1,98	0,67
7	975Pav2X8	1	39,52		4,84		11,57		10,57		0,14		13,80		11,75		2,37		1,00		*nd*	*nd*	95,55	0,78	2,05	0,70
	975Pav2X7	4	39,30	*0,64*	4,90	*0,30*	11,85	*0,36*	10,91	*0,63*	0,30	*0,13*	13,00	*0,30*	11,49	*0,10*	2,54	*0,02*	1,07	*0,08*	*nd*	*nd*	95,66	0,81	2,06	0,69
8	975Pav1.5X8	1	38,80		4,67		12,09		11,09		0,20		13,20		11,55		2,64		1,18		*nd*	*nd*	95,44	0,88	2,11	0,68
	975Pav1.5X7	3	39,40	*0,50*	4,99	*0,20*	11,24	*0,34*	11,14	*0,69*	0,20	*0,08*	13,52	*0,33*	11,49	*0,02*	2,52	*0,14*	1,13	*0,08*	*nd*	*nd*	95,63	0,87	2,07	0,69

[a]For the natural amphiboles, core or rim analyses; * for data from Bourdier (1980) and ** for cumulate analyses; For the experimental amphiboles, run number as in Table 3. All oxides in wt%, with number of analyses (**n**) and statistical errors (italic numbers) for the experimental compositions. **A_Cat** and **Al^{IV}** give the cation number in the alkali site and the tetra-coordinated aluminium in p.f.u., respectively, calculated after Leake et al. (1997) on a H_2O-free 23 oxygen basis with iron as FeO. **Mg#** gives the magnesium number as molar $Mg/(Mg+Fe_{tot})$; *nd* for not determined.

B3. Clinopyroxene

Type[a]	Sample#	n	SiO_2	TiO_2	Al_2O_3	FeO	MnO	MgO	CaO	Na_2O	K_2O	P_2O_5	F	Total	Wo	En	Fs	Mg#
Natural (selected)																		
core	PAV-1-02-1		50,43	0,27	1,81	10,14	0,85	12,60	22,60	0,83	0,01	0,00	0,00	99,53	46,69	36,22	17,09	0,70
rim	PAV-1-02-6		50,09	0,70	2,55	8,55	0,54	12,72	22,79	0,81	0,04	0,00	0,00	98,78	48,16	37,40	14,44	0,73
core	PAV-P1-14-3		50,66	0,37	1,80	9,42	1,10	12,13	22,39	0,96	0,00	0,00	0,00	98,82	47,43	35,77	16,80	0,71
rim	PAV-P1-15-2		49,04	1,12	3,84	9,38	0,35	13,05	22,51	0,67	0,00	0,00	0,22	100,18	46,92	37,85	15,22	0,72
core	P20-P1-04		50,45	0,34	2,30	10,76	0,62	12,19	21,92	0,96	0,01	0,00	0,00	99,54	46,21	35,76	18,03	0,68
core	P20-P1-19		49,08	1,18	3,74	8,41	0,27	13,54	22,11	0,68	0,00	0,02	0,00	99,02	46,58	39,70	13,72	0,75
core	P20-P1-27		49,01	1,06	3,68	8,73	0,50	13,10	22,09	0,75	0,00	0,00	0,00	98,92	46,75	38,57	14,68	0,74
core*	6		49,70	0,55	2,92	10,93	0,52	11,22	21,72	1,17	0,00	*nd*	*nd*	98,73	47,29	33,99	18,72	0,66
core*	7		48,19	1,38	5,99	5,09	0,14	14,59	21,61	0,50	0,00	*nd*	*nd*	97,49	47,15	44,29	8,56	0,84
rim*	8		50,19	1,15	4,22	6,11	0,07	15,36	20,96	0,44	0,00	*nd*	*nd*	98,50	44,63	45,51	9,86	0,82
rim*	9		49,32	1,23	4,48	7,01	0,17	14,38	21,59	0,47	0,00	*nd*	*nd*	98,65	45,95	42,59	11,46	0,79
core*	11		46,94	2,09	7,13	7,57	0,07	12,87	21,94	0,66	0,00	*nd*	*nd*	99,27	48,14	39,30	12,57	0,76
core*	12		51,02	0,63	2,71	8,58	0,26	13,22	22,68	0,72	0,00	*nd*	*nd*	99,82	47,54	38,56	13,90	0,74
rim*	13		49,43	0,81	2,91	9,53	0,61	12,25	22,38	1,02	0,00	*nd*	*nd*	98,94	47,57	36,23	16,20	0,70

core**	Cum1_14		45,20		2,20		7,65		8,29		0,16		12,91		20,06		0,56		0,00	0,00	0,00	97,02	45,21	40,49	14,29	0,74
core**	Cum1_15		45,25		2,51		8,15		7,77		0,07		12,40		20,98		0,63		0,00	0,00	0,10	97,87	47,56	39,12	13,32	0,75
core**	Cum1_16		46,56		2,11		6,88		8,21		0,24		13,34		20,23		0,63		0,01	0,00	0,00	98,21	44,83	41,12	14,05	0,75
core**	Cum3_5		49,23		1,23		3,92		7,73		0,26		15,59		19,36		0,43		0,00	0,00	0,09	97,82	41,15	46,11	12,74	0,79
core**	Cum3_7		45,70		2,13		7,31		7,96		0,00		13,13		21,29		0,46		0,00	0,00	0,19	98,18	46,77	40,14	13,09	0,75
core**	Cum3_8		47,52		1,98		5,09		6,68		0,00		14,18		20,70		0,59		0,06	0,03	0,00	96,83	45,56	43,42	11,01	0,80
core**	Cum3_10		48,46		1,73		5,47		7,62		0,05		14,51		20,58		0,54		0,00	0,00	0,19	99,15	44,24	43,39	12,37	0,78
core**	Cum3_11		49,76		1,13		4,38		7,13		0,20		15,37		20,67		0,38		0,00	0,00	0,00	99,02	43,46	44,99	11,56	0,80
Experimental (average)																										
3	850Pav3X8	1	46,74		1,33		5,15		12,94		0,81		9,36		20,70		0,92		0,25	0,05	0,01	96,33	46,97	29,56	23,47	0,57
	850Pav3X7	3	49,66	*1,58*	0,86	*0,07*	4,64	*0,54*	9,84	*0,86*	0,65	*0,23*	10,49	*0,57*	20,01	*1,05*	0,87	*0,04*	0,41	0,06	0,08	97,59	47,09	34,35	18,57	0,66
4	950Pav2X1ox	3	45,96	*0,93*	1,73	*0,39*	6,64	*1,10*	8,83	*0,60*	0,38	*0,12*	13,57	*0,16*	19,58	*1,64*	1,12	*0,30*	0,37	0,08	0,22	98,48	43,11	41,64	15,25	0,74
	950Pav2X7ox	4	49,64	*0,35*	1,24	*0,17*	5,57	*0,64*	9,79	*1,77*	0,63	*0,14*	11,50	*0,92*	19,66	*0,55*	0,91	*0,07*	0,48	0,10	0,01	99,62	45,20	36,79	18,02	0,69
6	950Pav2X7	2	47,25	*0,96*	1,28	*0,26*	5,42	*0,69*	9,28	*1,27*	0,73	*0,03*	12,02	*0,07*	21,84	*0,50*	0,71	*0,04*	0,20	0,40	0,00	99,09	47,39	36,31	16,30	0,71
8	975Pav1.5X8	3	47,91	*0,40*	1,49	*0,06*	3,60	*0,22*	9,24	*0,51*	0,41	*0,05*	13,55	*0,37*	20,76	*0,08*	0,49	*0,04*	0,17	*nd*	*nd*	97,62	44,03	40,22	15,75	0,73
	975Pav1.5X7	4	48,24	*0,40*	1,44	*0,10*	4,21	*0,60*	9,68	*1,09*	0,49	*0,21*	12,56	*0,51*	20,02	*0,53*	0,60	*0,09*	0,26	*nd*	*nd*	97,51	44,34	38,74	16,92	0,71

[a]For the natural clinopyroxenes, core or rim analyses; * for data from Bourdier (1980) and ** for cumulate analyses; For the experimental clinopyroxenes, run number as in Table 3. All oxides in wt%, with number of analyses (**n**) and statistical errors (italic numbers) for the experimental compositions. **Wo**, **En**, and **Fs** give the wollastonite, enstatite, and ferrosilite mole %, respectively; **Mg#** gives the magnesium number as molar Mg/(Mg+Fe_{tot}); *nd* for not determined.

B4. Biotite

Type[a]	**Sample#**	**n**	**SiO_2**		**TiO_2**		**Al_2O_3**		**FeO**		**MnO**		**MgO**		**CaO**		**Na_2O**		**K_2O**		**P_2O_5**	**F**	**Total**	**Mg#**
Natural (selected)																								
in Am_P20-P1-38	P20-P1-34		35,74		5,95		13,51		14,42		0,32		14,41		0,02		0,76		9,00		0,07	0,13	94,33	0,65
in Am_P20-P1-38	P20-P1-35		35,28		6,48		13,34		14,78		0,16		14,82		0,08		0,93		8,83		0,00	0,00	94,69	0,65
in Am_P20-P1-38	P20-P1-36		36,32		5,96		14,11		14,85		0,17		14,20		0,02		0,86		8,71		0,40	0,11	95,33	0,64
in Am_P20-P1-38	P20-P1-37		36,21		5,97		14,24		14,53		0,33		14,56		0,03		0,82		8,67		0,04	0,36	95,75	0,65
Microlite*	12		35,76		2,50		17,76		19,53		0,19		10,24		0,01		0,34		10,01		*nd*	*nd*	96,34	0,49
Experimental (average)																								
1	900Pav3X1	3	35,73	*0,72*	4,43	*0,12*	15,63	*0,27*	13,44	*0,03*	0,13	*0,06*	15,64	*0,63*	0,09	*0,04*	0,96	*0,04*	8,11	*0,08*	0,07	0,01	94,24	0,68
	900Pav3X8	1	34,73		5,09		15,75		14,49		0,09		14,66		0,04		0,88		8,28		0,00	0,41	94,40	0,65
	900Pav3X7	3	35,93	*0,22*	5,85	*0,16*	14,57	*0,16*	15,77	*1,30*	0,25	*0,01*	12,43	*0,54*	0,22	*0,12*	0,88	*0,17*	8,07	*0,50*	0,14	0,69	94,80	0,58
2	950Pav3X1	2	38,83	*0,03*	3,62	*0,10*	14,53	*0,24*	16,76	*2,51*	0,13	*0,01*	11,67	*2,20*	0,50	*0,06*	0,91	*0,11*	7,81	*0,36*	0,10	0,54	95,40	0,56
	950Pav3X8	3	35,91	*0,69*	5,51	*0,13*	15,41	*0,19*	12,26	*0,36*	0,08	*0,02*	15,30	*0,16*	0,04	*0,03*	0,96	*0,07*	8,11	*0,27*	0,05	0,00	93,62	0,70
	950Pav3X7	1	38,51		6,27		16,73		13,14		0,03		12,49		0,04		0,83		8,49		0,00	0,02	96,55	0,64
3	850Pav3X1	3	35,84	*0,41*	4,19	*0,08*	15,09	*0,22*	13,46	*0,39*	0,23	*0,09*	14,68	*0,56*	0,11	*0,04*	1,01	*0,09*	8,25	*0,03*	0,06	0,08	92,99	0,67

	850Pav3X8	3	35,66	*0,80*	4,84	*0,19*	14,52	*0,56*	15,08	*0,28*	0,13	*0,12*	13,66	*0,66*	0,19	*0,13*	0,75	*0,05*	8,40	*0,16*	0,05	0,22	93,50	0,60
	850Pav3X7	4	37,74	*2,18*	4,94	*0,29*	14,17	*0,30*	14,68	*1,08*	0,30	*0,13*	12,07	*1,18*	0,58	*0,61*	1,03	*0,41*	8,12	*0,35*	0,19	0,20	94,03	0,60
4	950Pav2X7ox	4	35,95	*0,20*	5,85	*0,19*	14,27	*0,32*	10,75	*0,27*	0,21	*0,08*	16,81	*0,43*	0,13	*0,06*	0,94	*0,01*	8,26	*0,20*	0,02	0,22	93,41	0,74
5	900Pav4X1	4	35,74	*0,49*	4,18	*0,09*	15,99	*0,14*	13,27	*0,43*	0,15	*0,06*	15,20	*0,28*	0,11	*0,06*	0,87	*0,08*	8,53	*0,24*	*nd*	*nd*	94,05	0,68
	900Pav4X8	2	36,77	*1,40*	4,93	*0,19*	16,08	*0,49*	14,89	*0,09*	0,17	*0,24*	13,23	*1,15*	0,06	*0,02*	0,78	*0,00*	8,34	*0,40*	*nd*	*nd*	95,25	0,62
	900Pav4X7	3	35,42	*0,49*	5,64	*0,17*	14,69	*0,33*	15,75	*0,52*	0,19	*0,06*	13,33	*0,10*	0,45	*0,50*	0,82	*0,02*	8,64	*0,08*	*nd*	*nd*	94,94	0,61
6	950Pav2X1	3	35,47	*0,22*	5,98	*0,30*	15,39	*0,22*	11,33	*0,68*	0,17	*0,06*	16,16	*0,68*	0,07	*0,05*	0,06	*0,06*	8,50	*0,14*	*nd*	*nd*	94,10	0,73
	950Pav2X8	4	36,81	*1,17*	5,93	*0,53*	15,13	*0,14*	11,66	*0,67*	0,16	*0,08*	15,01	*0,54*	0,23	*0,20*	1,07	*0,15*	8,36	*0,56*	*nd*	*nd*	94,36	0,71
	950Pav2X7	4	36,42	*1,37*	6,11	*0,10*	14,97	*0,44*	12,89	*0,92*	0,12	*0,10*	14,58	*0,77*	0,26	*0,19*	0,99	*0,06*	8,27	*0,30*	*nd*	*nd*	94,62	0,68

[a]For the natural biotites, inclusions in amphibole or microlite in the matrix; * for data from Bourdier (1980); For the experimental biotites, run number as in Table 3. All oxides in wt%, with number of analyses (**n**) and statistical errors (italic numbers) for the experimental compositions. **Mg#** gives the magnesium number as molar Mg/(Mg+Fe_{tot}); *nd* for not determined.

B5. Fe-Ti oxides

Type[a]	Sample	n	SiO_2	TiO_2	Al_2O_3	FeO	MnO	MgO	CaO	Na_2O	K_2O	Total	Mt-Ilm
Natural (selected)													
in Cpx	PAV-P1-01-4		0,04	11,44	2,43	78,23	0,95	2,61	0,16	0,00	0,05	95,91	Mt67
in Cpx	PAV-1-01-6		0,02	9,56	2,20	81,56	1,28	1,97	0,05	0,00	0,04	96,69	Mt72
in Cpx	PAV-1-02-2		0,03	36,59	0,30	56,73	0,82	2,61	0,11	0,00	0,00	97,19	Ilm65
in Cpx	PAV-1-02-3		0,00	37,43	0,31	55,27	0,83	2,72	0,21	0,00	0,05	96,81	Ilm67
in Cpx	PAV-1-02-4		0,13	7,41	1,59	82,87	1,01	1,62	0,20	0,00	0,00	94,83	Mt78
in Cpx	PAV-1-02-5		0,14	7,81	1,79	81,69	1,15	1,84	0,15	0,08	0,00	94,64	Mt77
pheno	PAV-1-02-7		0,03	9,49	2,42	81,35	1,16	1,92	0,04	0,00	0,02	96,43	Mt72
in Am	PAV-P1-04-3		0,00	36,62	0,40	55,74	0,98	2,72	0,01	0,04	0,00	96,51	Ilm64
in Am	PAV-P1-04-6		0,07	38,26	0,32	55,02	0,83	2,81	0,08	0,00	0,03	97,42	Ilm68
in Am	PAV-P1-14-2		0,00	9,18	2,25	79,41	0,90	2,38	0,00	0,03	0,00	94,16	Mt73
pheno	P20-P1-08		0,06	9,19	2,28	79,30	0,77	2,21	0,01	0,00	0,00	93,82	Mt73
pheno	P20-P1-17		0,10	9,29	2,37	82,04	0,79	2,11	0,01	0,00	0,00	96,71	Mt73
pheno	P20-P1-18		0,04	35,95	0,36	56,00	1,04	2,86	0,01	0,00	0,03	96,28	Ilm64
in Cpx	P20-P1-31		0,09	9,14	2,13	80,03	0,97	2,27	0,06	0,00	0,02	94,71	Mt73
in Am	P20-P1-39		0,05	37,81	0,40	55,87	0,96	2,90	0,03	0,00	0,01	98,02	Ilm66
pheno	P20-P1-41		0,06	38,12	0,36	56,63	0,81	2,75	0,00	0,00	0,00	98,73	Ilm67
pheno*	6		0,03	9,32	2,53	81,24	1,02	2,36	0,05	0,00	0,00	96,55	Mt74
pheno*	7		0,08	8,92	2,38	80,63	1,07	2,00	0,01	0,00	0,00	95,10	Mt75
pheno*	11		0,00	38,34	0,39	54,46	0,82	2,64	0,01	0,00	0,00	96,66	Ilm70
pheno*	12		0,01	36,63	0,32	54,45	1,08	2,64	0,02	0,03	0,00	95,18	Ilm67

Experimental (average)																					
1	900Pav3X1	1	0,11		11,48		4,18		75,56		0,50		2,56		0,09		0,00		0,02		94,50	Mt65
		2	0,14	*0,03*	42,55	*0,74*	0,38	*0,04*	47,42	*0,86*	0,79	*0,00*	3,63	*0,19*	0,21	*0,05*	0,02	*0,03*	0,09	*0,03*	95,23	Ilm79
	900Pav3X8	2	0,13	*0,14*	11,76	*0,03*	4,19	*0,30*	73,65	*0,05*	0,65	*0,10*	2,40	*0,08*	0,06	*0,01*	0,02	*0,00*	0,04	*0,05*	92,90	Mt63
	900Pav3X7	2	0,21	*0,03*	12,67	*0,33*	3,00	*0,15*	74,15	*1,19*	0,98	*0,05*	1,88	*0,06*	0,13	*0,04*	0,00	*0,00*	0,07	*0,05*	93,09	Mt61
2	950Pav3X1	2	0,24	*0,00*	12,85	*0,30*	4,66	*0,02*	68,30	*0,91*	0,53	*0,00*	3,59	*0,24*	0,12	*0,02*	0,04	*0,06*	0,07	*0,03*	90,40	Mt60
	950Pav3X8	2	0,05	*0,06*	46,84	*0,74*	0,39	*0,03*	43,06	*0,86*	0,66	*0,00*	5,00	*0,08*	0,11	*0,01*	0,03	*0,03*	0,04	*0,05*	96,19	Ilm87
	950Pav3X7	1	0,16		14,94		4,93		68,94		0,55		2,82		0,15		0,09		0,07		92,65	Mt52
		2	0,11	*0,07*	46,58	*0,06*	0,39	*0,03*	44,01	*0,04*	0,73	*0,08*	4,04	*0,02*	0,15	*0,01*	0,02	*0,02*	0,09	*0,02*	96,13	Ilm87
3	850Pav3X1	3	0,37	*0,18*	7,93	*0,46*	3,44	*0,20*	75,34	*0,44*	0,75	*0,13*	2,15	*0,10*	0,18	*0,11*	0,05	*0,01*	0,1	*0,02*	90,31	Mt75
		2	0,39	*0,22*	37,72	*0,96*	0,57	*0,12*	50,74	*0,58*	0,92	*0,12*	2,83	*0,08*	0,17	*0,05*	0,02	*0,02*	0,1	*0,04*	93,46	Ilm71
	850Pav3X8	4	0,30	*0,17*	8,98	*0,17*	2,73	*0,14*	75,84	*0,63*	1,03	*0,14*	1,81	*0,04*	0,23	*0,09*	0,01	*0,01*	0,11	*0,07*	91,03	Mt72
	850Pav3X7	2	0,35	*0,05*	9,36	*0,34*	2,36	*0,11*	77,12	*0,32*	1,02	*0,24*	1,76	*0,07*	0,22	*0,12*	0,01	*0,02*	0,05	*0,00*	92,25	Mt
4	950Pav2X1ox	5	0,21	*0,16*	25,30	*1,09*	0,91	*0,12*	61,98	*1,88*	0,38	*0,16*	2,69	*0,52*	0,15	*0,06*	0,01	*0,01*	0,08	*0,02*	91,71	Hem
		2	0,19	*0,03*	5,48	*0,15*	3,91	*0,03*	77,86	*0,83*	0,78	*0,08*	4,17	*0,20*	0,16	*0,07*	0,00	*0,00*	0,08	*0,08*	92,64	Mt83
	950Pav2X7ox	3	0,48	*0,37*	26,93	*0,38*	0,81	*0,05*	59,98	*0,70*	0,52	*0,05*	2,94	*0,05*	0,21	*0,04*	0,03	*0,03*	0,17	*0,02*	92,08	Hem
		1	0,15		6,80		3,43		78,99		0,94		3,92		0,08		0,03		0,05		94,38	Mt84
5	900Pav4X1	3	0,24	*0,10*	8,51	*0,12*	4,07	*0,15*	77,09	*0,80*	0,71	*0,14*	2,33	*0,08*	0,15	*0,05*	0,02	*0,02*	0,08	*0,04*	93,20	Mt74
	900Pav4X8	2	0,21	*0,01*	9,25	*0,14*	3,69	*0,08*	76,41	*0,66*	0,85	*0,09*	2,08	*0,00*	0,23	*0,14*	0,00	*0,00*	0,08	*0,02*	92,79	Mt72
		1	0,11		40,97		0,50		50,12		1,14		2,75		0,20		0,00		0,13		95,91	Ilm76
	900Pav4X7	1	0,35		10,10		2,82		75,40		1,24		1,81		0,27		0,02		0,13		92,13	Mt70
6	950Pav2X1	1	0,30		14,33		4,42		69,46		0,76		3,81		0,14		0,00		0,02		93,23	Mt56
		3	0,20	*0,12*	46,51	*0,58*	0,43	*0,06*	43,78	*0,59*	0,69	*0,17*	4,94	*0,13*	0,14	*0,04*	0,02	*0,01*	0,10	*0,03*	97,10	Ilm85
	950Pav2X8	3	0,20	*0,04*	13,67	*1,52*	4,89	*0,50*	68,44	*0,54*	0,73	*0,17*	3,90	*0,03*	0,11	*0,08*	0,02	*0,01*	0,08	*0,03*	92,04	Mt57
		1	0,20		46,69		0,42		44,02		0,78		5,30		0,20		0,00		0,10		97,71	Ilm84
7	975Pav2X1	3	0,07	*0,07*	8,99	*0,21*	4,35	*0,16*	74,02	*0,60*	0,50	0,09	3,74	*0,10*	0,10	*0,01*	0,02	*0,01*	0,08	*0,05*	91,87	Mt72
	975Pav2X9	2	0,09	*0,01*	9,91	*0,19*	4,83	*0,03*	72,70	*0,77*	0,51	0,27	3,95	*0,07*	0,09	*0,06*	0,01	*0,01*	0,06	*0,08*	92,13	Mt69
	975Pav2X8	3	0,13	*0,01*	11,40	*0,32*	4,87	*0,09*	70,34	*0,51*	0,62	0,15	4,09	*0,17*	0,14	*0,04*	0,02	*0,03*	0,05	*0,07*	91,65	Mt64
	975Pav2X7	3	0,10	*0,05*	12,64	*0,32*	3,99	*0,08*	71,37	*0,92*	0,68	0,05	3,98	*0,06*	0,07	*0,03*	0,02	*0,02*	0,02	*0,01*	92,88	Mt61
8	975Pav1.5X1	2	0,07	*0,02*	9,42	*0,22*	4,62	*0,01*	75,09	*0,93*	0,52	0,05	3,97	*0,09*	0,08	*0,05*	0,05	*0,01*	0,04	*0,05*	93,86	Mt71
	975Pav1.5X9	2	0,13	*0,11*	10,84	*0,15*	4,47	*0,18*	71,99	*2,41*	0,44	0,04	4,44	*0,19*	0,09	*0,04*	0,00	*0,00*	0,02	*0,02*	91,41	Mt66
	975Pav1.5X8	3	0,39	*0,15*	12,53	*0,37*	4,29	*0,30*	69,41	*0,56*	0,71	0,12	4,40	*0,14*	0,08	*0,05*	0,01	*0,02*	0,10	*0,03*	91,94	Mt61
	975Pav1.5X7	3	0,18	*0,12*	12,61	*0,51*	4,07	*0,44*	69,37	*0,77*	0,70	0,05	4,29	*0,08*	0,09	*0,07*	0,00	*0,00*	0,05	*0,06*	91,38	Mt60

[a]For the natural Fe-Ti oxide, occurrence as phenocryst (pheno) or as inclusion in clinopyroxene (in Cpx) or amphibole (in Am); * for data from Bourdier (1980); For the experimental Fe-Ti oxides, run number as in Table 3. All oxides in wt%, with number of analyses (**n**) and statistical errors (italic numbers) for the experimental compositions. **Mt** and **Ilm** give the magnetite and ilmenite molar %, respectively, calculated after Sauerzapf et al. (2008); **Hem** for hematite.

B6. Glasses

Type[a]	Sample#	n	SiO_2		TiO_2		Al_2O_3		FeO		MnO		MgO		CaO		Na_2O		K_2O		P_2O_5	F	Total	H_2O
Natural (selected)																								
MG	P20-P1-09		64,79		0,62		17,33		3,12		0,16		0,38		1,52		6,07		5,99		0,00	0,03	97,67	0,8
MG	P20-P1-10		65,45		0,68		17,07		2,69		0,11		0,38		1,51		5,79		6,10		0,22	0,00	97,63	0,9
MG	P20-P1-11		65,40		0,71		16,47		3,10		0,20		0,44		1,23		5,80		6,38		0,17	0,09	98,06	0,6
MG	P20-P1-22		64,31		0,61		17,50		2,70		0,09		0,38		2,10		5,73		6,11		0,22	0,26	97,27	1,1
MG	P20-P1-28		66,19		0,74		16,86		2,65		0,15		0,41		1,39		5,50		6,11		0,01	0,00	96,93	1,3
MG	P20-P1-33		65,29		0,56		16,79		3,32		0,26		0,35		1,51		5,79		5,72		0,16	0,25	98,50	0,3
MG	P20-P1-42		65,05		0,74		17,54		2,61		0,01		0,41		1,60		5,98		5,56		0,01	0,48	98,58	0,3
GI in Cpx PAV-1-02-1	P20-P1-05		65,90		0,39		16,74		3,02		0,08		0,39		1,77		6,11		5,54		0,04	0,00	93,44	3,4
GI in Cpx PAV-1-02-1	P20-P1-06		66,42		0,64		16,67		2,95		0,32		0,35		1,83		4,88		5,65		0,30	0,00	90,58	5,3
GI in Cpx PAV-1-02-1	P20-P1-07		65,44		0,50		17,21		3,13		0,12		0,49		2,00		5,72		5,40		0,00	0,00	92,80	3,9
GI in Cpx PAV-P1-15-2	P20-P1-12		64,86		0,61		17,68		2,51		0,13		0,54		2,03		6,06		5,09		0,12	0,38	93,78	3,0
GI in Cpx PAV-P1-15-2	P20-P1-13		66,63		0,41		16,81		2,84		0,00		0,56		1,57		5,14		5,45		0,22	0,36	91,10	4,6
GI in Cpx PAV-P1-15-2	P20-P1-15		64,12		0,60		17,14		3,31		0,02		0,28		1,57		5,99		6,47		0,25	0,23	96,40	1,3
GI in Cpx P20-P1-19	P20-P1-20		65,05		0,71		17,70		2,40		0,19		0,48		1,87		5,85		5,59		0,16	0,00	93,48	3,4
GI in Cpx P20-P1-19	P20-P1-21		63,97		0,61		17,23		2,85		0,11		0,31		1,91		6,82		6,02		0,17	0,00	94,56	2,7
GI in Mt P20-P1-39	P20-P1-40		64,08		0,66		17,50		3,66		0,23		0,56		1,91		5,60		5,48		0,23	0,10	96,94	1,1
Experimental (average)																								
1	900Pav3X1	3	64,84	*1,07*	0,69	*0,19*	20,28	*0,14*	1,51	*0,31*	0,09	*0,02*	0,04	*0,02*	5,18	*0,21*	3,59	*0,12*	3,26	*0,16*	0,21	0,30	88,47	
	900Pav3X8	1	65,56		0,69		20,34		1,18		0,06		0,00		4,44		3,60		3,99		0,12	0,00	88,87	
2	950Pav3X1	3	63,64	*1,37*	0,69	*0,20*	19,63	*0,17*	1,92	*0,90*	0,10	*0,04*	0,05	*0,01*	5,89	*0,11*	4,57	*0,27*	2,73	*0,03*	0,61	0,17	89,46	
	950Pav3X8	2	64,30	*1,96*	0,62	*0,42*	19,70	*0,14*	1,71	*0,90*	0,16	*0,04*	0,08	*0,09*	5,77	*0,23*	4,44	*1,21*	2,68	*0,25*	0,13	0,41	90,01	
3	850Pav3X1		68,73	*0,22*	0,41	*0,17*	19,60	*0,27*	0,99	*0,39*	0,07	*0,06*	0,04	*0,01*	3,69	*0,10*	2,62	*0,31*	3,51	*0,15*	0,09	0,25	85,83	
	850Pav3X8		67,68	*0,18*	0,57	*0,09*	18,12	*0,28*	2,28	*0,21*	0,11	*0,07*	0,31	*0,12*	2,45	*0,03*	4,07	*0,06*	4,25	*0,17*	0,06	0,10	88,77	
	850Pav3X7		71,63	*0,26*	0,43	*0,01*	17,63	*0,27*	1,51	*0,05*	0,10	*0,01*	0,08	*0,06*	1,37	*0,38*	2,91	*0,00*	4,24	*0,45*	0,03	0,09	87,16	
4	950Pav2X1ox		63,36	*0,60*	0,85	*0,08*	18,55	*0,40*	2,94	*0,06*	0,13	*0,06*	1,09	*0,05*	3,23	*0,11*	4,92	*0,34*	4,58	*0,10*	0,29	0,05		
	950Pav2X7ox		64,34	*0,52*	0,88	*0,10*	17,55	*0,42*	2,88	*0,34*	0,12	*0,11*	1,06	*0,26*	2,61	*0,42*	5,47	*0,34*	4,96	*0,19*	0,04	0,09		
5	900Pav4X1		65,30	*0,20*	0,50	*0,08*	20,78	*0,11*	1,13	*0,16*	0,18	*0,07*	0,09	*0,04*	4,46	*0,10*	4,01	*0,15*	3,48	*0,09*	0,07	*nd*		
	900Pav4X8		69,94	*3,92*	0,33	*0,10*	18,92	*1,37*	0,84	*0,41*	0,12	*0,09*	0,01	*0,07*	2,06	*1,78*	3,87	*0,91*	3,83	*0,45*	0,07	*nd*		
7	975Pav2X1	3	59,69	*0,29*	1,38	*0,06*	19,02	*0,25*	4,74	*0,26*	0,16	*0,12*	1,69	*0,06*	4,92	*0,07*	4,50	*0,27*	3,91	*0,14*	*nd*	*nd*	90,07	
	975Pav2X9	2	59,41	*0,12*	1,42	*0,04*	19,03	*0,26*	4,75	*0,32*	0,20	*0,13*	1,70	*0,05*	4,97	*0,06*	4,78	*0,12*	3,75	*0,06*	*nd*	*nd*	91,60	
	975Pav2X8	3	59,52	*0,24*	1,30	*0,03*	18,84	*0,29*	4,66	*0,27*	0,05	*0,05*	1,71	*0,03*	4,90	*0,11*	5,03	*0,07*	3,98	*0,14*	*nd*	*nd*	92,22	
	975Pav2X7	3	60,71	*0,10*	1,14	*0,02*	18,25	*0,07*	4,54	*0,19*	0,21	*0,07*	1,50	*0,01*	3,91	*0,10*	5,24	*0,21*	4,50	*0,27*	*nd*	*nd*	93,42	

8	975Pav1.5X1	2	59,59	*0,81*	1,27	*0,18*	19,19	*0,19*	4,77	*0,55*	0,03	*0,04*	1,76	*0,14*	4,84	*0,00*	4,80	*0,01*	3,74	*0,19*	*nd*	*nd*	90,82
	975Pav1.5X9	3	60,03	*0,80*	1,15	*0,16*	18,62	*0,43*	4,64	*0,15*	0,13	*0,03*	1,73	*0,05*	4,63	*0,28*	4,98	*0,12*	4,09	*0,10*	*nd*	*nd*	91,43
	975Pav1.5X8	1	60,40		1,23		18,47		4,69		0,16		1,65		3,82		4,95		4,63		*nd*	*nd*	93,18
	975Pav1.5X7	4	61,77	*0,25*	0,97	*0,07*	17,97	*0,27*	4,30	*0,17*	0,13	*0,02*	1,43	*0,04*	3,23	*0,04*	5,14	*0,06*	5,07	*0,15*	*nd*	*nd*	92,42

[a]For the natural glasses, **MG** for matrix glass and **GI** for glass inclusion; For the experimental glasses, run number as in Table 3. All oxides in wt% recalculated to 100 wt%, with Na_2O corrected by a factor 1.2. The number of analyses (**n**) and the statistical errors (italic numbers) are given for the experimental compositions. **Total** gives the raw sum of the analysed oxides without Na correction. **H_2O** gives the water contents of the natural glasses determined by the 'by-difference' method, as defined in text ('Analytical method' section); *nd* for not determined.

Appendix C (Thermobarometry).

C1. Two-oxides thermo-oxymetry after Sauerzapft et al. (2008).

Sample[a]	log(Mg/Mn)[b]		Sauerzapft et al. (2008)		
	Mt	Ilm	T °C	log fO2	NNO
Selected natural (Mt/Ilm)					
PAV-P1-01-4/ PAV-P1-04-6	0.68	0.77	969	-9.42	+1.3
PAV-P1-02-4/ PAV-P1-04-6	0.45	0.77	851	-10.94	+1.8
Experimental					
900PAV3X1 (NNO +0.8)	0.95	0.91	901	-10.95	+0.9
950PAV3X7 (~NNO +1)	0.95	0.99	924	-11.26	+0.2
850PAV3X1 (NNO +0.8)	0.70	0.73	870	-10.85	+1.5
900PAV4X8 (~NNO +1)	0.63	0.63	860	-11.25	+1.3
950PAV2X1 (NNO +0.7)	0.95	1.10	924	-11.13	+0.4
950PAV2X8 (NNO +0.5)	0.97	1.08	926	-10.99	+0.4

[a] For the experimental samples, run conditions are given in Table 3 and **Mt-Ilm** are taken as the average compositions given in Appendix B5**.**

[b] Chemical equilibrium test after Bacon and Hirschmann (1988), i.e. log(Mg/Mn) in Mt and Ilm compares within an error of ±0.20.

C2. Amphibole thermo-baro-oxy-hygrometry after Ridolfi and Renzulli (2012).

Sample	check	$T_{\pm 22}$ (°C)	ΔT (°C)	P (MPa)	Pσ (MPa)	ΔP (MPa)	NNO	$H2O_{melt}$ (wt%)	H2Oσ	ΔH2O (wt%)
Experimental										
900Pav3X1	ok	1016	116	536	59	236	-0,2	5,4	0,8	
900Pav3X8	ok	1030	130	573	63	273	-0,2	5,2	0,8	
950Pav3X8	ok	1026	76	510	56	210	-0,2	4,5	0,7	
950Pav3X7	ok	991	41	405	45	105	-0,4	4,5	0,7	
850Pav3X1	ok	996	146	481	53	181	-0,1	5,0	0,8	
850Pav3X8	wrong	invalid		invalid	invalid		invalid	invalid	invalid	
950Pav2X1ox	ok	1009	59	383	42	183	0,6	3,5	0,5	
950Pav2X8ox	ok	991	41	338	37	138	0,5	3,0	0,5	
950Pav2X1	ok	1030	80	504	55	304	-0,1	4,5	0,7	
950Pav2X8	ok	1012	62	416	46	216	0,0	3,9	0,6	
950Pav2X7	ok	996	46	381	42	181	-0,2	3,8	0,6	
900Pav4X8	ok	1039	139	670	74	270	-0,2	6,0	0,9	
900Pav4X7	ok	1015	115	546	60	146	-0,3	5,0	0,7	
Natural										
PAV-P1-01-1	ok	1028		461	51		-0,8	4,3	0,6	
PAV-P1-01-2	ok	980		338	37		-0,4	3,3	0,5	
PAV-P1-04	ok	1007		367	40		-0,4	3,2	0,5	
PAV-P1-04-2	ok	1020		334	37		-0,1	2,5	0,4	
PAV-P1-04-5	ok	984		347	38		-0,4	3,1	0,5	
PAV-P1-05-1	ok	990		368	40		-0,5	3,2	0,5	
PAV-P1-14-1	ok	997		376	41		-0,6	3,6	0,5	

P20-P1-32	ok	1028	487	54	-0,6	3,7	0,5
P20-P1-38	ok	989	338	37	-0,3	2,6	0,4
PavP115bo	ok	992	387	43	-0,5	3,7	0,6
PavP115co	ok	985	340	37	-0,4	3,2	0,5
6*	ok	1025	525	58	-0,7	4,8	0,7
7*	wrong	invalid	invalid	invalid	invalid	invalid	invalid
8*	ok	1010	452	50	-0,5	3,8	0,6
9*	ok	1014	490	54	-0,6	4,4	0,7
10*	ok	1075	638	70	-0,6	4,7	0,7
11*	ok	1009	432	48	-0,4	3,8	0,6
Pavin_Cum1_1	ok	1054	616	68	-0,6	5,2	0,8
Pavin_Cum1_3	ok	1062	787	87	-1,1	6,5	1,0
Pavin_Cum1_4	ok	1050	564	62	-0,4	4,5	0,7
Pavin_Cum1_5	ok	1049	606	67	-0,5	5,0	0,8
Pavin_Cum3_1	ok	1067	707	78	-0,7	5,3	0,8
Pavin_Cum3_2	ok	1053	599	66	-0,6	4,8	0,7

[a] Run conditions as given in Table 3 and calculations after the amphibole composition given in Appendix B2; * for data from Bourdier (1980).

Appendix D (Phase-equilibrium run).

D1. Phase relationships

In order to constrain the storage conditions of the Pavin trachyandesite, experimental conditions were chosen to cover the range of intensive parameters inferred from the natural assemblage. Therefore, phase equilibrium experiments were performed from 850 to 950 °C, 150 to 400 MPa, NNO+1 and +2, and X_{H2Oin} ranging between 0.7 and 1 (melt H_2O contents from 4.5 to 9.5 wt%) (Table 3).

At 365 MPa, 900 °C, and ~NNO+1.5, biotite, magnetite, ilmenite, and rare apatite are present at H_2O-saturation conditions (~9.5 wt% H_2O) in proportion of ~16 wt% (Fig. 9a). Amphibole and plagioclase appear for H_2O contents around 8-9 wt% (Fig. 9b), with an increase of crystallinity to ~40 wt%, and clinopyroxene replaces amphibole for H_2O contents $\leq$ 8 wt% (~70 wt% crystallinity; Fig. 9c).

At ~300 MPa and NNO+0.5 to +1.0, biotite and magnetite are liquidus phases at 950 °C and H_2O-saturated conditions, with possibly amphibole (~8.5 wt% H_2O, ~16 wt% crystallinity; Fig. 9a). Ilmenite crystallize for ~8 wt% H_2O (~23 wt% crystallinity; Fig. 9a), followed by plagioclase for ~7 wt% H_2O (~70 wt% crystallinity; Fig. 9c). At 900 °C, the assemblage of biotite, magnetite, ilmenite, amphibole, and apatite prevailing at H_2O saturation (~16 wt% crystallinity; Fig. 9a) is completed by plagioclase for $\leq$8 wt% H_2O (~22 wt% crystallinity; Fig. 9b). Clinopyroxene replaces amphibole for H_2O contents $\leq$7 wt% (~70 wt% crystallinity; Fig. 9c). At 850 °C, biotite, amphibole, magnetite, ilmenite, and plagioclase are stable at H_2O-saturation conditions (~35 wt% crystallinity; Fig. 9a), clinopyroxene appears between 7.5 and 8.5 wt% H_2O (~40 wt% crystallinity; Fig. 9b) whereas amphibole disappears for H_2O contents below 7.0-7.5 wt% (~63 wt% crystallinity; Fig. 9c).

At ~200 MPa, 975 °C and ~NNO+1, magnetite is the liquidus phase at H_2O saturation (~7 wt%; Fig. 9a), followed by amphibole and plagioclase for H_2O contents $\leq$6 wt% (~4% and ~15 wt% crystallinity for ~6.0 and ~5.5 wt% H_2O, respectively; Fig. 9b-c). At 950 °C and NNO+1, the experiment failed after about two days, showing evidence of incomplete maturation of the minerals (e.g. hollow plagioclases). Yet, although total crystallinities and the residual glass compositions cannot be used, the crystal assemblages and compositions may be relevant to the imposed *P-T* conditions. In this experiment, magnetite, ilmenite, amphibole, plagioclase, biotite, and apatite are present for H_2O contents from saturation to ~6.5 wt% (Fig. 9a-b), followed by clinopyroxene for H_2O contents <6 wt% (Fig. 9c). An additional

experiment was performed at 950 °C under f_{O2} conditions of NNO+2, in which magnetite, hematite, amphibole, plagioclase, and clinopyroxene are present at H_2O saturation condition (~24 wt% crystallinity; Fig. 9a). Biotite appears for H_2O contents of 6-7 wt% (~76 wt% crystallinity; Fig. 9c), highlighting the predominance of clinopyroxene at NNO+2 at the expense of biotite at NNO+1.

D2. Phase compositions

The experimental plagioclase ranges from $An_{36}Or_{10}$ at low pressure and H_2O contents ~5.5 wt% to $An_{55}Or_2$ at liquidus conditions at 300 MPa. The plagioclase An content increases with increasing T and H_2O content (Fig. 3; B1), in agreement with previous studies (e.g. Martel et al., 1999).

The clinopyroxene ranges from $Wo_{43}En_{42}$ in oxidized conditions (NNO+2, 950 °C, 200 MPa) to $Wo_{47}En_{34}$ at 300 MPa, 850 °C and NNO+1 (Fig. 5a), with Mg# ranging from 0.57 to 0.74. The clinopyroxene Al_2O_3 content (4.6 to 6.6 wt%) is inversely correlated to SiO_2 content (46 to 50 wt%), and globally decreases with decreasing P and increasing T (Fig. 5b; B3).

Biotite shows 14-17 wt% Al_2O_3 (B4) and Mg# from 0.56 at liquidus condition, 300 MPa, and NNO+1 to 0.74 for the NNO+2 experiment at 200 MPa (Fig. 6).

The amphiboles contain from 11 wt% Al_2O_3 at low T and 300 MPa to 14 wt% Al_2O_3 at 400 MPa (B2). They show numbers of cation in the A_site ranging from 0.73-0.78 at 200 MPa to 0.78-0.98 at 300-400 MPa, with Al^{IV} ranging from 1.93 to 2.20 after the calculation of Leake et al. (1997) (Fig. 4).

Fe-Ti oxides are magnetite and ilmenite in the NNO+1 experiments, with total range compositions of Mt_{52-75} and Ilm_{71-87}. At NNO+2, Mt_{83-84} coexists with hematite (B5).

The residual glasses show SiO_2 contents from 63 to 72 wt%, with a clear compositional difference depending on P. Indeed, 150-200 MPa residual glasses are trachyandesitic (59-64 wt% SiO_2 and 8.5-10.5 wt% Na_2O+K_2O) whereas the 300-400 MPa glasses are dacitic to rhyolitic (64-72 wt% SiO_2 and 6-8 wt% Na_2O+K_2O) (Fig. 7; B6).

Reference

Martel, C., Pichavant, M., Holtz, F., Scaillet, B., Bourdier, J.-L., Traineau, H., 1999. Effect of fO_2 and H_2O on andesite phase relations between 2 and 4 kbars. J. Geophys. Res. 104, 29453-29470.